Conformational dynamics of auto-inhibition in the ER calcium sensor STIM1

Stijn van Dorp[1], Ruoyi Qiu[1], Ucheor B. Choi[1,3], Minnie M. Wu[1], Michelle Yen[1], Michael Kirmiz[1], Axel T. Brunger[1,2], and Richard S. Lewis[1]*

[1]Department of Molecular and Cellular Physiology, Stanford University School of Medicine, Stanford, CA 94305

[2]Howard Hughes Medical Institute, Stanford University School of Medicine, Stanford, CA 94305, USA

[3]Present address: Department of Biochemistry, West Virginia University School of Medicine, Morgantown, WV 2650

*email: rslewis@stanford.edu

Abstract

The dimeric ER Ca^{2+} sensor STIM1 controls store-operated Ca^{2+} entry (SOCE) through the regulated binding of its CRAC activation domain (CAD) to Orai channels in the plasma membrane. In resting cells, the STIM1 CC1 domain interacts with CAD to suppress SOCE, but the structural basis of this interaction is unclear. Using single-molecule Förster resonance energy transfer (smFRET) and protein crosslinking approaches, we show that CC1 interacts dynamically with CAD in a domain-swapped configuration with an orientation predicted to sequester its Orai-binding region adjacent to the ER membrane. Following ER Ca^{2+} depletion and release from CAD, cysteine crosslinking indicates that the two CC1 domains become closely paired along their entire length in the active Orai-bound state. These findings provide a structural basis for the dual roles of CC1: sequestering CAD to suppress SOCE in resting cells and propelling it towards the plasma membrane to activate Orai and SOCE after store depletion.

Introduction

Store-operated Ca^{2+} entry (SOCE) is a nearly ubiquitous signaling pathway activated by extracellular stimuli that deplete Ca^{2+} from the endoplasmic reticulum (ER). SOCE is essential for many physiological functions of excitable and non-excitable cells, including gene expression, secretion, and motility (Prakriya and Lewis, 2015). Accordingly, loss-of-function mutations in the core SOCE components lead to serious human pathologies, including severe combined immunodeficiency, autoimmunity, myopathy, ectodermal dysplasia and anhidrosis (Lacruz and Feske, 2015), while gain-of-function mutations cause Stormorken syndrome, miosis, myopathy, thrombocytopenia and excessive bleeding (Böhm and Laporte, 2018). These clinical manifestations underscore the need for precise regulation of SOCE to ensure that it is silent when ER Ca^{2+} stores are full yet reliably activated by stimuli that drive store depletion.

The ER membrane protein STIM1 (Figure 1a, top) controls SOCE through the regulated interaction of its CRAC activation domain (CAD (Park et al., 2009); also known as SOAR (Yuan et al., 2009) or CCb9 (Kawasaki et al., 2009)) with Orai1 Ca^{2+} channels in the plasma membrane. In resting cells, Ca^{2+} bound to the luminal EF hands of the STIM1 dimer suppresses STIM1 activity by promoting intramolecular association of the coiled-coil 1 (CC1) domains with CAD, referred to as the 'inhibitory clamp' (Korzeniowski et al., 2010; Fahrner et al., 2014; Ma et al., 2015; Yang et al., 2012; Yu et al., 2013). Upon ER Ca^{2+} depletion, dissociation of Ca^{2+} from the luminal EF hands triggers conformational changes that release CC1 from CAD and promotes STIM1 accumulation at ER-plasma membrane (ER-PM) junctions where the CAD domain binds, traps, and activates Orai1 channels diffusing in the PM (Liou et al., 2007; Wu et al., 2014, 2006). Thus, to elucidate the regulatory mechanism of SOCE, it is essential to understand how CC1 interacts with CAD to control STIM1 activity.

36 The CC1 domain comprises three helical segments, CC1α1-3 (Soboloff et al., 2012)
37 (Figure 1a). Current evidence suggests that CC1α1, the most ER-proximal segment, acts as a
38 bimodal switch to stabilize both the quiescent and active states of STIM1. When ER Ca^{2+} stores
39 are full, CC1α1 binds to the CAD CC3 helix to sequester CAD (Fahrner et al., 2014; Ma et al.,
40 2015); upon store depletion, the luminal EF-SAM domains dimerize, CC1α1 unbinds from CAD,
41 and the transmembrane and proximal CC1α1 regions form a coiled-coil (Stathopulos et al., 2006;
42 Schober et al., 2019; Hirve et al., 2018), projecting CAD towards the plasma membrane.
43 Although several residues in CC1α1 and CC3 have been identified as essential for forming the
44 inhibitory clamp (Fahrner et al., 2014; Muik et al., 2011; Zhou et al., 2013; Ma et al., 2015), the
45 helical arrangement of the CC1α1:CAD binding interface is completely unknown. In addition,
46 while CC1α3 is implicated in stabilizing the inactive state (Yang et al., 2012; Korzeniowski et
47 al., 2010), it is unclear whether this results from binding to CAD or another mechanism (Zhou et
48 al., 2013).
49 Attempts to determine the structure of full-length STIM1 in the inactive or active state
50 have been unsuccessful. Instead, structures of several fragments from the STIM1 cytosolic
51 region have offered potential clues, although it is not yet clear how they might relate to
52 physiological states of the full-length protein. The crystal structure of human STIM1 CAD (aa
53 345-444, with mutations L374M, V419A, and C437T) depicts a parallel V-shaped dimer
54 comprising CC2 and CC3 domains (Figure 1a, bottom left) (Yang et al., 2012). It is unknown
55 whether this structure represents an active or inactive conformation, and the absence of CC1
56 precludes inferences about its interaction with CAD. A solution NMR structure of a CC1α3-
57 CC2 fragment depicts a dimer of wedged antiparallel CC2 helices (Figure 1a, bottom right)
58 (Stathopulos et al., 2013). This NMR structure can bind Orai1 C-terminal fragments *in vitro* and

59 has been proposed to be an intermediate in the activation of STIM1 (Stathopulos et al., 2013),
60 but to our knowledge it has never been shown to bind intact Orai1 channels *in situ* and lacks the
61 CC3 helix needed to evoke SOCE (Covington et al., 2010). Finally, in a crystal structure of CC1
62 (aa 237-340, with mutations M244L and L321M), two elongated CC1 helices form an
63 antiparallel coiled-coil dimer within the CC1α2 and CC1α3 domains (see Figure 5d (Cui et al.,
64 2013), but it is unclear how this elongated structure with its widely separated C-termini could
65 attach to the closely paired N-termini of CAD.

66 Although the sequences of these three structures partially overlap, their conformations are
67 incompatible with each other, raising fundamental questions about their potential relation to the
68 inactive and active forms of STIM1. What is the conformation of CAD in the context of the
69 entire cytosolic domain? How is CC1 arranged relative to CAD in the inactive state, and how
70 does this change during activation? Which regions of STIM1 are stable, and which are flexible?
71 To address these questions, we examined the structure and dynamics of the full cytosolic domain
72 of STIM1 (ctSTIM1, aa 233-685) using single-molecule Förster resonance energy transfer
73 (smFRET) measurements at sites throughout CC1 and CAD. smFRET is commonly applied to
74 estimate intramolecular distances and reveal asynchronous molecular transitions that are
75 typically obscured in population measurements. Our results show that CAD in ctSTIM1
76 resembles the CAD crystal structure, but with unexpected structure and flexibility in an apical
77 region that is critical for Orai binding and activation. CC1α1 interacts with CAD in a domain-
78 swapped configuration to form the inhibitory clamp, enabled by the arrangement of the CC1α2
79 and CC1α3 domains. The Stormorken mutation R304W activates ctSTIM1 by releasing CC1α1
80 from CAD. In studies of full-length STIM1 in intact cells, state-dependent cysteine crosslinking
81 after store depletion suggests that after unbinding from CAD, the two CC1 domains pack

82 together along their entire length, in contrast to the CC1 crystal and CC1α3-CC2 NMR
83 structures. Together, these findings offer the first structural view of the STIM1 inhibitory clamp
84 and reveal the massive conformational changes evoked by store depletion, which serve to
85 reorient and translocate CAD towards the PM where it can bind Orai1 and activate SOCE.

Results

The CC2 domains in ctSTIM1 are oriented in a parallel configuration

We initially applied smFRET to test whether the conformation of CAD within the cytosolic domain (ctSTIM1, aa 233-685) resembles that of the CC2-CC3 crystal structure (Yang et al., 2012) or the CC1α3-CC2 NMR structure (Stathopulos et al., 2013), referred to below as the 'crystal structure' or 'NMR structure,' respectively. A major distinction between the two structures is that the CC2 domains (aa 345-391) in CAD are parallel in the crystal structure but antiparallel in the NMR structure (Figure 1a). After removing the single native cysteine in ctSTIM1 with a C437S mutation, we created three mutants with cysteines at positions 337, 363, and 378, for which the two structures predicted very different inter-subunit distances, particularly for 337:337′ and 378:378′ (hereafter ':' is used to denote a pair of sites in the dimer and '′' indicates a site on the adjacent subunit) (Figure 1a). The ctSTIM1 mutants were expressed in *E. coli* and purified, yielding full-length protein of >90% purity (see Methods). After randomly labeling the cysteine-mutant ctSTIM1 molecules with FRET donor (Alexa Fluor 555) and acceptor (Alexa Fluor 647) dyes, single ctSTIM1 dimers were surface-tethered to a glass coverslip for imaging by TIRF microscopy, either encapsulated in liposomes or attached directly through a tag on the C-terminus (Figure 1b; the attachment method for each measurement is shown in Supplementary Figure 1). Upon excitation of the donor dye, the donor and acceptor emissions of individual molecules were ratioed to calculate FRET efficiencies, which were high and stable at all three label sites (Figure 1c and 1d). These results are consistent with a CAD conformation in which the CC2 domains are closely apposed and parallel, as in the crystal structure. Inter-fluorophore distances calculated from simulations of the donor and acceptor dye positions on the crystal structure (see Methods) closely matched those derived from smFRET,

109 while simulations based on the NMR structure deviated substantially (Figure 1e). We conclude
110 that in the context of the complete ctSTIM1 in solution, the CC2 domains in CAD adopt a
111 parallel conformation consistent with the CAD crystal structure and not the NMR structure.
112
113 **The apex of CAD deviates from the crystal structure**
114 We made additional smFRET measurements throughout the entire CAD to allow a more
115 complete comparison with the crystal structure. Near the C-terminal end of the CC3 domain (aa
116 408-437), the 431:431′ label pair produced a stable, narrowly defined high-FRET state (Figure
117 2a), and inter-subunit smFRET throughout the CAD exceeded 0.5, consistent with a compact
118 parallel dimer (Figure 2b). Near the dimer interface (hereafter termed the 'base' of CAD),
119 smFRET-derived distances quantitatively agreed with those from the crystal structure, and an
120 intra-subunit measurement 431:363 directly confirmed the compact folding of CC3 onto CC2
121 within each subunit (Figure 2c).
122 In contrast to the base of CAD, smFRET measurements of the distal CC2 and CC2-CC3
123 linker regions (the CAD 'apex') deviated from those indicated in the crystal structure (Figure
124 2d). This is particularly interesting as mutagenesis studies have identified this region as critical
125 for Orai1 binding and activation (Calloway et al., 2010; Korzeniowski et al., 2010; Thompson et
126 al., 2018; Butorac et al., 2019; Wang et al., 2014). To provide a rough indication of the extent of
127 the deviation implied by smFRET, we generated an alternative model of the CAD apex based on
128 the crystal structure by allowing rotation around G379 to bring the simulated FRET efficiencies
129 in line with our experimental results. In the resulting model the distal CC2 regions were rotated
130 outward, while the regions around aa 400 were pulled closer together, effectively compacting the
131 apical 'V-shape' (Figure 2e and see Methods). Whereas inter-subunit smFRET at aa 399-401

132 appeared as a well-defined peak, FRET levels at the distal end of CC2 were broadly distributed
133 and appeared multimodal, particularly at aa 388 (Figure 2b). Accordingly, smFRET
134 measurements in this region displayed occasional fluctuations (Figure 2f), suggesting
135 conformational flexibility that was not expected from the uninterrupted rigid helix of the crystal
136 structure. The smFRET-derived model in Figure 2e thus likely represents just one of a number
137 of potential apical conformations sampled by spontaneous fluctuations of the distal CC2 domain.
138 As a complementary structural test, we analyzed inter-subunit cysteine-cysteine (cys-cys)
139 crosslinking upon oxidation by copper phenanthroline (CuP, see Methods). Cysteines introduced
140 throughout the CAD apex formed inter-subunit crosslinks, detected as ctSTIM1 dimers on non-
141 reducing SDS-PAGE gels (Supplementary Figure 2a). This result shows that opposing residues
142 in the apical region at least transiently come within the ~6 Å range for cys-cys crosslinking (Qin
143 et al., 2015), again inconsistent with the CAD crystal structure. Moreover, crosslinking
144 efficiencies were similar for three adjacent apical cysteine pairs (399:399′, 400:400′, and
145 401:401′), suggesting significant rotational flexibility beyond the temporal resolution of our
146 smFRET recordings. Taken together, these data show that flexibility and spontaneous
147 fluctuations cause the CAD apical region to deviate significantly from the crystal structure,
148 unlike the stable basal region.
149
150 **CC1α1 docks parallel to CC3 in a domain-swapped configuration**
151 The CC1 domain controls the activation of STIM1 *in vivo* by releasing CAD for interaction with
152 Orai1 (Zhou et al., 2013; Ma et al., 2015). Although it is clear that the membrane-proximal
153 CC1α1 domain can interact with CAD to inhibit STIM1 (Ma et al., 2015), their relative
154 orientations remain undefined. We detected high inter-subunit FRET efficiencies between labels

155 at the N-termini of CC1α1 and CC3 (red histogram in Figure 3a, top), as well as between labels
156 at their C-termini (blue histogram in Figure 3a, bottom), indicating that the CC1α1 domain (a
157 continuous α-helix (Cui et al., 2013; Rathner et al., 2020)) is oriented parallel to CC3 in the
158 predominant ctSTIM1 conformation.

159 To determine whether CC1α1 associates with the CAD of the same subunit or the
160 adjacent one within the dimer, we compared inter-subunit and intra-subunit FRET efficiencies
161 between labels at the N-terminus of CC1α1 and three sites in CAD (Figure 3b). The
162 predominant inter-subunit FRET efficiencies were consistently higher than intra-subunit FRET
163 efficiencies, demonstrating that in the predominant ctSTIM1 conformation, CC1α1 engages
164 CAD in a domain-swapped configuration. We also observed spontaneous and reversible
165 transitions from the predominant FRET state, in which FRET efficiencies fluctuated between the
166 same two levels for both inter- and intra-subunit measurements (Figure 3c). Similar fluctuation
167 behavior and transition kinetics were observed at all three CAD sites (Supplementary Figure 3a),
168 suggesting a conformational transition in which the two CC1α1 domains briefly switch sides on
169 CAD, probably using the same binding interface (Figure 3d).

170

171 **The CC1α3 domains are compactly folded and directed away from CAD**

172 *In vivo*, mutations or deletions of the CC1α3 domain activate STIM1 (Korzeniowski et al., 2010;
173 Yang et al., 2012) but the underlying mechanism, in particular the proposal that CC1α3 interacts
174 directly with CAD (Yang et al., 2012), has been questioned (Zhou et al., 2013). We measured
175 predominantly high inter-subunit FRET efficiencies of ~0.9 between labels at the N- and C-
176 terminal ends of the CC1α3 domains (aa 312 and 337, respectively), indicating that the two
177 domains are closely apposed and parallel (Figure 4a). To determine their orientation relative to

178 CAD, we measured intra-subunit FRET efficiencies between labels at either end of the CC1α3
179 domain to three sites in CC2. While FRET efficiency from the CC1α3 C-terminus to the
180 proximal CC2 domain was high as expected (red histogram in Figure 4b, top), low FRET
181 efficiencies were measured from the CC1α3 N-terminus, indicating that the N-terminus is
182 directed away from CAD (Figure 4b, bottom).
183 Stable high inter-subunit FRET efficiencies at the CC1α3 C-terminus (aa 337) were
184 consistent with its proximity to the compact, stable CAD base. However, label sites near the N-
185 terminus of CC1α3 displayed brief (0.8 s average lifetime), large transitions to a low FRET state,
186 suggesting that the N-termini of CC1α3 intermittently splay out from a stable pivot point at the
187 base of CAD (Figure 4c, d). While these large conformational transitions were most common,
188 further analysis revealed additional substates in the smFRET trajectories (Supplementary Figure
189 3b, c).
190
191 **A model for the CC1-CAD complex**
192 Through the integration of many inter-molecular distance measurements, smFRET can be
193 applied to build models of tertiary protein structure (Brunger et al., 2011). We used 36 unique
194 inter- and intra-subunit smFRET measurements to develop a structural model of the resting
195 conformation of CC1 subdomains relative to the optimized model of CAD depicted in Figure 2e.
196 Each CC1 domain in the ctSTIM1 dimer was modeled as a set of three rigid α-helical domains
197 connected by flexible linkers, consistent with bioinformatic analysis (Soboloff et al., 2012),
198 NMR measurements of the CC1 fragment (Rathner et al., 2020), and distances estimated from
199 intra-subunit smFRET efficiencies (239:274, 274:307, and 307:337; Supplementary Figure 1).
200 We selected randomly generated models that met the criteria of satisfying smFRET-derived

201 distance constraints while avoiding steric clashes with each other or with CAD (see Methods and
202 Supplementary Figure 4a, c for details of the modeling process). Two classes of models
203 emerged that were highly similar but distinguishable by the organization of the CC1α2/3
204 domains. In ~70% of solutions the CC1α2/3 domains were stacked parallel (representative
205 model in Figure 5a from an ensemble of models shown in Supplementary Figure 4bi), while the
206 remaining solutions had an alternative, wedged CC1α2/3 topology (Figure 5a and Supplementary
207 Figure 4bii). Importantly, both classes of solutions displayed the defining features described
208 above, including closely apposed CC1α3 domains directed away from CAD and CC1α1 domains
209 oriented parallel to CC3 in a domain-swapped configuration.

210 As an independent test of the smFRET-derived models, we applied the lysine
211 crosslinking agent BS^3 combined with mass spectrometry (XLMS) to identify residues in close
212 proximity to each other (Rappsilber, 2011). BS^3 XLMS confirmed key structural arrangements
213 of both models of the CC1-CAD complex, including the compact packing of CC1α2/3 domains
214 and the domain-swapped CC1α1-CAD interaction (Supplementary Figure 5a-e).

215 Although the models do not specify the orientation of side chains in the CC1 helices, they
216 highlight two regions for potential inter-subunit coiled-coil interactions in the CC1-CAD
217 complex: an antiparallel apposition of heptad repeats in CC1α2 and CC1α3′ (Figure 5b) and a
218 parallel apposition of heptad repeats in CC1α1 and CC3′ (Figure 5c). The CC1α2/α3′ interface
219 is reminiscent of the tight, antiparallel interaction of CC1α2 and CC1α3′ domains in the CC1
220 dimer crystal structure (Cui et al., 2013), an arrangement that was further supported by the
221 formation of amine-carboxy crosslinks in ctSTIM1 by 1-ethyl-3-(3-
222 dimethylaminopropyl)carbodiimide hydrochloride (EDC), a zero-length crosslinker (Figure 5d
223 and Supplementary Figure 6).

224 Interestingly, the CC1α1:CC3′ interface in the smFRET-derived models juxtaposes
225 multiple hydrophobic residues that have been previously implicated through mutagenesis in
226 stabilizing the CC1-CAD complex: L248, L251, L258, L261 in CC1α1 and L416, V419, and
227 L423 in CC3 (Fahrner et al., 2014; Muik et al., 2011; Zhou et al., 2013; Ma et al., 2015). To
228 refine the CC1α1:CC3′ interface, we aligned the crystal structure of the CC1α1 domain (aa 246-
229 271) to the smFRET-derived model and performed a computational docking simulation using
230 Rosetta software. The resulting model indicates an extensive pairing of hydrophobic residues
231 predicted to stabilize the CC1α1:CC3′ interface (Figure 5e), providing a plausible explanation
232 for the activating effects of disruptive mutations at these sites.
233
234 **The Stormorken mutation R304W activates ctSTIM1 by releasing CC1α1 from CAD**
235 The close packing of CC1α1 and CAD in our model suggests that ctSTIM1 is primarily inactive.
236 Accordingly, when expressed with Orai1 in HEK293 cells, mCh-ctSTIM1 only slightly
237 increased $[Ca^{2+}]_i$ compared to mCh-CAD (Supplementary Figure 7), in agreement with previous
238 evidence that ctSTIM1 is a relatively weak activator of Orai1 (Park et al., 2009; Korzeniowski et
239 al., 2010; Yuan et al., 2009; Muik et al., 2009).
240 Deletion of the CC1 domain (mCh-ctSTIM1-ΔCC1) restored ctSTIM1 activity to the
241 level seen with CAD, as did the introduction of R304W, a naturally occurring mutation that
242 causes Stormorken syndrome by constitutively activating STIM1 (Misceo et al., 2014; Morin et
243 al., 2014; Nesin et al., 2014) (Supplementary Figure 7). Interestingly, introduction of R304W
244 into ctSTIM1 almost completely eliminated the high inter-subunit FRET between CC1α1 sites
245 and the CC3 N-terminus *in vitro*, indicating the release of CC1α1 from CAD (Figure 6a, left and

246 center). A more moderate decrease in FRET efficiency was observed relative to the CC3 C-
247 terminus (aa 431), suggesting that CC1α1 pivoted around the CC1α1/2 linker (Figure 6a, right).
248 To determine how R304W releases the CC1α1 domain given its distant location at the C-
249 terminal end of CC1α2, we examined its effect on folding of the CC1α2 and CC1α3 domains.
250 Intra-subunit smFRET measurements indicated that R304W increases the separation between the
251 CC1α2 N-terminus and the CC1α3 C-terminus (274:337) (Figure 6a, bottom left), suggesting it
252 has opened the tight angle between CC1α2 and CC1α3. R304W also shifted CC1α2:CC1α2′ and
253 CC1α3:CC1α3′ FRET to lower levels (Figure 6b), again consistent with opening of the compact
254 inactive structure.
255 The R304W mutation also significantly altered the structural dynamics of CC1α2/α3. In
256 the wild-type protein, the predominant inter-subunit FRET efficiency at the CC1α3 N-terminus
257 was high, interrupted by occasional transitions to a low FRET state (Figure 4c and Figure 6c,
258 left). In contrast, the R304W mutation appeared to destabilize the CC1α3 pair, such that it
259 transitioned between high and low FRET through a series of intermediates states (Figure 6c,
260 right). Taken together, our data reveal several effects of R304W on the CC1 domain: it
261 destabilizes the tight packing of CC1α3 domains, causes CC1α2 to splay out from CC1α3, and
262 completely releases CC1α1 from CAD.
263 We also assessed effects of R304W on the structure of CAD. While the R304W mutation
264 or the deletion of CC1 (ΔCC1) did not affect inter-subunit FRET efficiencies at the base of CAD
265 (431:431′), they did alter the smFRET distributions at the CAD apex (389:389′ and 400:400′)
266 (Figure 6d). Together, these results suggest that the association of CC1α1 with CAD influences
267 the conformation of the flexible apex without affecting the arrangement of helices at the more
268 stable CAD base.

269

270 **The CC1 domains refold into a parallel dimer during STIM1 activation**

271 We applied cysteine crosslinking to obtain complementary structural information for the CC1
272 domains. Inter-subunit cysteine crosslinking in ctSTIM1 was notably robust in the CC1α2/α3
273 linker (aa 307) and the C-terminus of CC1α3 (aa 339) (Supplementary Figure 8a). Disulfide
274 formation at T307C prevented BS^3 from crosslinking CC1α1 and CAD, indicating that T307C
275 crosslinking is incompatible with the CC1α1-CAD inhibitory clamp (Supplementary Figure 5f).
276 Similar findings were obtained for the activated ctSTIM1 mutants R304W and L248S/L251S
277 (Supplementary Figure 5f), suggesting that close apposition and crosslinking at T307C resulted
278 from spontaneous, transient visits to an activated state of ctSTIM1.

279 Under physiological conditions, full-length STIM1 (flSTIM1) in cells is activated by Ca^{2+}
280 store depletion. To extend our *in vitro* ctSTIM1 results to flSTIM1, we examined cysteine
281 crosslinking of inactive and active flSTIM1 *in vivo*. Cysteine mutations in flSTIM1 were made
282 at selected sites throughout CC1, transiently expressed in HEK293 cells, and treated with the
283 cell-permeant oxidizer diamide before or after store depletion induced by cyclopiazonic acid
284 (CPA). Lysates of diamide-treated cells were then analyzed for the presence of crosslinked
285 flSTIM1 dimers. Prior to store depletion, when flSTIM1 is inactive, little crosslinking was
286 observed throughout CC1, with the exception of S339C near the junction with CAD (Figure 7a
287 and 7b). In contrast, after store depletion prominent crosslinking occurred at A268C and T307C
288 in addition to S339C (Figure 7a and 7b, Supplementary Figure 8). These results further support
289 our conclusion above that T307C crosslinking of ctSTIM1 *in vitro* is enabled by transient
290 activation events. More importantly, they suggest that activation *in vivo* brings all three CC1
291 subdomains together.

292 To test this idea, we asked whether cysteine crosslinking after ER Ca^{2+} store depletion
293 could lock flSTIM1 in the activated state, thereby preventing deactivation of STIM1 and SOCE
294 upon store refilling. Ionomycin was added in Ca^{2+}-free Ringer's to deplete stores, after which
295 ionomycin was removed and Ca^{2+} readded to allow Ca^{2+} influx through SOCE. In HEK cells
296 expressing WT flSTIM1, $[Ca^{2+}]_i$ increased rapidly upon Ca^{2+} readdition and subsequently
297 declined due to store refilling and deactivation of STIM1 and Orai1, regardless of diamide
298 treatment (Figure 7c). We obtained a similar result with flSTIM1-S339C, indicating that
299 diamide-induced crosslinking at S339C does not impede flSTIM1 deactivation. In contrast,
300 crosslinking at A268C and T307C prevented the normal deactivation of SOCE as indicated by
301 the sustained elevation of $[Ca^{2+}]_i$ after Ca^{2+} readdition. These findings suggest that all three CC1
302 subdomains are brought close together during STIM1 activation *in vivo* and remain closely
303 associated in the final, Orai1-bound conformation (Figure 7d).

304 **Discussion**

305 Precise regulation of SOCE is essential for many physiological processes and is achieved
306 through control of transitions between inactive and active states of STIM1. These transitions are
307 triggered by changes in ER [Ca^{2+}] that toggle reversible interactions of the STIM1 CC1 domain
308 with CAD. Through a combination of smFRET measurements and crosslinking assays, we have
309 determined the arrangements of CC1 and CAD helices in inactive and active states of STIM1.
310 The results reveal how CC1 is oriented around CAD to stabilize the inactive state, and how its
311 conformation changes upon activation to project CAD toward the PM to engage Orai1 and
312 trigger SOCE.

313 In this study, we measured FRET efficiencies from single ctSTIM1 dimers to generate an
314 overlapping set of intramolecular distance constraints for modeling tertiary structure (Choi et al.,
315 2010; Brunger et al., 2011). Caution must be applied in using FRET signals to infer absolute
316 distances, as FRET efficiency can also be affected by photophysical transitions or interactions
317 with the local environment (Weiss, 1999, 2000). We employed several strategies to avoid
318 misinterpretation of the data. First, by including a large number of different FRET pairs (36
319 pairs for CC1-CAD), no major feature of the CC1-CAD model was dependent on any single
320 measurement, safeguarding against potential problems with individual label sites (Supplementary
321 Figure 4a, c). Second, we independently verified the CC1-CAD model by mass spectrometry
322 analysis of BS^3-crosslinked protein (Schmidt and Robinson, 2014) (Supplementary Figure 5a-e).
323 Third, measurements of key smFRET amplitudes and spontaneous structural transitions were
324 confirmed at multiple nearby sites (Figure 2 and Supplementary Figure 3). Finally, we applied
325 relatively conservative distance error limits (±1 nm) in constraining the CC1-CAD model. These
326 strategies taken together help validate the tertiary structures represented in our models.

327

328 **The conformation of CAD in the context of ctSTIM1**

329 smFRET measurements demonstrated that CAD within the context of ctSTIM1 resembles the
330 CAD crystal structure rather than the NMR structure of CC1α3-CC2 (Figure 1). The base is
331 stable and compact (Figure 2), as expected given the hydrophobic interactions and hydrogen
332 bonding between the two CAD subunits in this region (Yang et al., 2012). However, the CAD
333 apex appeared flexible and diverged from the crystal structure (Figure 2). These differences
334 most likely arose from stabilization of an alternate apical conformation in the crystal by
335 hydrogen bonds between the apex and adjacent CAD subunits (Supplementary Figure 1b) (Yang
336 et al., 2012). The flexible structure of the CAD apex we observed is intriguing because
337 mutagenesis and cysteine-crosslinking studies suggest this region interacts with Orai1 to initiate
338 channel activation (Calloway et al., 2010; Korzeniowski et al., 2010; Thompson et al., 2018;
339 Butorac et al., 2019; Wang et al., 2014), and conformational flexibility can facilitate protein-
340 protein interactions through effects on the thermodynamics of binding (Grünberg et al., 2006).
341 Thus, it is likely that the CAD apex in complex with Orai adopts a structure different from that
342 depicted in the CAD crystal and distinct from the NMR structure of CC1α3-CC2 (see below).
343 Release of CC1α1 from CAD, or deletion of the CC1 domain altogether, did not cause a gross
344 change in CAD structure, although it did alter the conformation of the CAD apex (Figure 6).
345 This raises the possibility that upon CC1α1 dissociation the apex changes shape, perhaps
346 facilitating its binding to Orai1.

347

348 **Defining structural roles for all three CC1 subdomains in the STIM1 inhibitory clamp**

349 Our results reveal how the three helical regions within CC1 collaborate to regulate the activity of
350 STIM1. Prior evidence indicated that CC1 autoinhibits STIM1 in resting cells but left
351 unanswered fundamental questions surrounding its structure. Korzeniowski and colleagues
352 originally reported that neutralization of acidic residues in the CC1α3 domain activated STIM1
353 and proposed an 'inhibitory clamp' mechanism in which this region binds to a basic region
354 within CAD to shield it from Orai in resting cells (Korzeniowski et al., 2010). This hypothesis
355 potentially explained the activation of STIM1 by deletion of the CC1α3 domain (Yang et al.,
356 2012). However, subsequent studies showed that CC1α3 alone is not sufficient to maintain the
357 inactive state, as CC1α3-CAD is fully active (Zhou et al., 2013); moreover, intermolecular FRET
358 between ER-tethered STIM1 fragments showed that CC1α1 can bind to CC3 (Fahrner et al.,
359 2014), and ER-tethered CC1α1 by itself can bind CAD and keep it from binding to Orai1 in the
360 PM (Fahrner et al., 2014; Ma et al., 2015). These findings and the activating effects of mutations
361 in CC1α1 (Fahrner et al., 2014; Muik et al., 2011; Zhou et al., 2013; Ma et al., 2015) and CC3
362 (Muik et al., 2011) shifted the focus to a CC1α1-CC3 interaction as the basis for the inhibitory
363 clamp, and the requirement for CC1α3 has remained unexplained. In addition to defining the
364 CC1α1-CC3 interaction (below), our smFRET-derived structure can now clarify why deletion of
365 CC1α3 disables the inhibitory clamp. CC1α2 and CC1α3 are compactly folded and directed
366 away from CAD, allowing CC1α1 to engage CC3 (Figure 5); in the absence of CC1α3, the rigid
367 CC1α2 helix would prevent CC1α1 from binding to CAD, which would then be free to interact
368 with Orai1. Consistent with this explanation, deletion of CC1α2 in addition to CC1α3 allows the
369 inhibitory clamp to function normally (Fahrner et al., 2014).
370 Based largely on mutagenesis studies, Zhou and colleagues proposed that the inhibitory
371 clamp results from antiparallel binding of CC1α1 to CC3, involving interactions between L261

372 and L416 and between L258 and V419 (Ma et al., 2015). In contrast, our smFRET
373 measurements show that CC1α1 binds parallel to CC3 (Figure 3). Moreover, our model depicts
374 interactions of L248 and L251 (CC1α1) with L416 (CC3), and of L258 and L261 (CC1α1) with
375 L423 and L427 (CC3) (Figure 5), which may explain the activating effects of non-conservative
376 mutations at these sites (Fahrner et al., 2014; Muik et al., 2011; Zhou et al., 2013; Ma et al.,
377 2015). Interestingly, our data reveal that CC1α1 preferentially associates with CC3 of the
378 adjacent subunit in the CAD dimer (Figure 3). Such a domain-swapped configuration may
379 enhance the stability of the inactive state through inter-subunit interactions and could promote
380 cooperativity between subunits during structural transitions.

381 Consistent with a high degree of flexibility, CC1 displayed large spontaneous FRET
382 fluctuations. The CC1α2/α3 domains occasionally transitioned from a compact, high-FRET
383 resting state to a low-FRET open state (Figure 4), while the CC1α1 domains briefly switched
384 sides on CAD, probably trading binding interfaces (Figure 3). Differences in dwell times
385 suggest these two types of fluctuations occurred independently (Supplementary Figure 3), but
386 further studies will be needed to determine how they relate to structural changes during
387 activation of membrane-inserted flSTIM1. During the preparation of this manuscript, a report
388 appeared describing a solution NMR structure of the isolated CC1 peptide, in which the
389 CC1α1/α2/α3 helices form a monomeric three-helix bundle (Rathner et al., 2020). Rathner et al
390 have proposed that this structure represents a pre-activated state of CC1 in which the interaction
391 of CC1α1 and CC1α2 has destabilized the clamp formed by CC1α1 and CC3. Our smFRET
392 experiments show that when CC1α1 associates with CC3 in ctSTIM1, the CC1α2 and CC1α3
393 domains primarily interact with each other to form a compact bundle pointing away from CAD

394 (Figure 5); in the context of this recent report, we hypothesize that the fluctuations of CC1α2/α3
395 we observed may represent spontaneous transitions into such a pre-activated state.
396 The R304W Stormorken mutation activates ctSTIM1 (Supplementary Figure 7),
397 consistent with its ability to activate flSTIM1 (Fahrner et al., 2018; Nesin et al., 2014; Morin et
398 al., 2014; Misceo et al., 2014). smFRET measurements show that R304W destabilizes the
399 compact packing of CC1α2/3 domains, increasing the angle between CC1α2 and CC1α3 helices
400 and fully releasing CC1α1 from CAD (Figure 6). These results are consistent with NMR studies
401 showing that R304W causes N-terminal extension of the CC1α3 helix, thereby stiffening the
402 CC1α2/α3 linker (Fahrner et al., 2018; Rathner et al., 2020).
403
404 **A structural view of quiescent STIM1 and its transition to the activated state**
405 Our results provide a first view of how the CC1 domain of STIM1 sequesters CAD near the ER
406 membrane in resting cells to prevent it from interacting with Orai. The parallel arrangement of
407 CC1α1 and CC3 in our smFRET-derived structure predicts that the CAD apex of inactive STIM1
408 is juxtaposed to the ER membrane and pointed away from the PM *in vivo* (Figure 8a). This
409 orientation implies that to activate STIM1 and SOCE, the CAD apex must rotate through a large
410 angle (up to 180°) and translocate more than 10 nm towards the PM - a massive conformational
411 change reminiscent of the refolding and extension of viral envelope proteins like hemagglutinin
412 when stimulated to trigger membrane fusion (Harrison, 2008). Hirve et al. showed that
413 activation of the flSTIM1 cytosolic domain is initiated by formation of a coiled-coil in the TM
414 domains and the proximal part of CC1α1 up to L251 (Hirve et al., 2018). As an extension to
415 these findings, we found that after store depletion, inter-subunit disulfide bonds form at A268C
416 (C-terminus of CC1α1) and T307C and S339C (N- and C-termini of CC1α3, respectively; Figure

417 7 and Supplementary Figure 8). Taken together, these results suggest that all three helical
418 domains in CC1 are closely paired in the active dimer, which would effectively move CAD
419 across the ~15 nm gap of the ER-PM junction to reach Orai (Wu et al., 2006).

420 Our CC1-CAD model specifies the possible types of conformational changes that must
421 occur to activate flSTIM1 and present the CAD apex to Orai (Figure 8b). We can envision two
422 potential solutions. In a 'flip-out' mechanism, CAD rotates as a whole by 180°. Although our
423 smFRET data indeed indicate that release of CC1α1 does not cause a gross conformational
424 change in CAD (Figure 6), this kind of CAD rotation would imply a complex asymmetric
425 intermediate, in which one of the C-terminal domains (aa 449-685) downstream of CAD would
426 need to be threaded between the two CC1 domains. Alternatively, in a 'fold-out' model, CAD
427 undergoes a symmetric conformational change while moving its apex away from the ER
428 membrane. This model posits that during activation the CC2 domains rotate to transiently
429 assume an antiparallel state, reminiscent of the NMR structure (Figure 1a and 8b). It is
430 important to note that our cysteine crosslinking results indicate the CC1α3 C-termini are closely
431 apposed in the Orai-bound state (Figure 7d, S339C), which is incompatible with the splayed
432 configuration of CC1α3 domains in the NMR structure. Thus, if the antiparallel conformation
433 exists it is likely to represent a transient intermediate during the activation of STIM1
434 (Stathopulos et al., 2013).

435 The ultimate endpoint in delineating the mechanism of SOCE is an atomic-level
436 description of the pathway of STIM1 activation by store depletion. To reach this goal the
437 starting, intermediate, and final conformations of STIM1 after store depletion must be resolved,
438 as well as the structure of the activated STIM-Orai complex. While approaches like cryo-EM
439 certainly offer an effective strategy for determining structures, time-resolved measurements such

440 as those afforded by smFRET will be essential to identify structural transitions in the activation
441 pathway. The results obtained thus far through smFRET of ctSTIM1 have revealed critical
442 measurement sites that offer a starting point for these studies. Ultimately, the identification of
443 transient intermediate STIM1 conformations and rate-limiting steps in the activation process may
444 reveal critical transitions that could be targeted to manipulate SOCE for therapeutic benefit.

445 ## Materials and methods

446 **DNA constructs.** For samples that were encapsulated in liposomes for surface immobilization,
447 DNA encoding ctSTIM1 (aa 233-685) was amplified by PCR from full-length human STIM1
448 (Origene), appending an N-terminal NcoI cleavage site, and a C-terminal TEV protease
449 recognition sequence (SENLYFQG) followed by a HindIII cleavage site. The ctSTIM1 insert
450 contained a silent T1764C mutation in H588 to remove an endogenous NcoI site, and a G1310C
451 mutation to replace the endogenous cysteine (C437S). ctSTIM1 inserts were ligated into the
452 pET28a vector which encoded a C-terminal 6-His tag. ctSTIM1 cysteine mutants were created
453 by site-directed mutagenesis (QuickChange II, Agilent). The translated ctSTIM1 protein
454 retained the sequence SENLYFQ at the C terminus after cleavage of the 6-His tag by TEV.

455 For samples that were directly attached to a PEG-coated surface, the pAC6 vector was
456 used with a C-terminal AviTag™ sequence GLNDIFEAQKIEWHE (Avidity). ctSTIM1 was
457 first ligated into a pTEV5 vector which encoded a TEV-cleavable N-terminal 6-His tag. DNA
458 encoding the 6-His tag, TEV recognition site and ctSTIM1 was then amplified by PCR,
459 appending an XhoI cleavage site to the N terminus, and a HindIII cleavage site to the C terminus
460 for ligation into the pAC6 vector. The resulting translated ctSTIM1 protein retained the N-
461 terminal sequence GAS after TEV cleavage of the 6-His tag, and it had the AviTag™ sequence
462 following a spacer KLPAGG on the C terminus. All constructs were verified by DNA
463 sequencing.

464

465 **Protein expression, purification, and labeling.** ctSTIM1 protein was expressed in *E. coli*
466 based on standard methods described previously (Choi et al., 2010). Briefly, plasmid containing
467 the ctSTIM1 insert was transformed to BL21 competent cells (New England Biolabs #C25271)

468 for pET28a plasmids, or CVB101 competent cells (Avidity #CVB101) for pAC6 plasmids.
469 Protein expression was induced with IPTG at OD ~0.4 in 450 ml Luria Broth (LB), and for
470 pAC6 plasmids biotin was added to a concentration of 50 µM. Bacteria were spun down and
471 then resuspended in denaturing PBS (8 M urea, 100 mM NaH_2PO_4, 10 mM Tris (pH 7.4 with
472 NaOH)) and lysed by sonication. TCEP (Thermo Fisher Scientific #77720) was added to a
473 concentration of 0.5 mM. For intra-subunit smFRET samples, double-cysteine ctSTIM1 was
474 mixed with cysteine-free ctSTIM1 in a 1:5 ratio to allow formation of ctSTIM1 heterodimers.
475 Samples were purified by NiNTA purification (Qiagen #30210), and subsequently slowly
476 dialysed using SnakeSkin™ (Life Technologies #68700) to 20/50 TBS (50 mM NaCl, 20 mM
477 Tris (pH 7.4 with HCl)) containing 1 mM DTT. TEV protease (MCLAB #TEV-200) was added
478 during dialysis at 10 µg/ml. Cleavage of the 6-His tag was usually almost 100%, as checked on
479 SDS page gel. Samples were further purified by ion exchange on a HiTrap Q column (GE
480 Healthcare Life Sciences #17-1153-01) and eluted in 250 µl aliquots of 20/250 TBS. All buffers
481 contained 0.5 mM TCEP. Resulting ctSTIM1 samples were >90% pure and displayed the
482 expected molecular weight (~52 kD) by SDS-PAGE. Dimer concentration was typically 25-50
483 µM, measured by absorption photometry (NanoDrop 2000, ThermoFisher Scientific).
484 Protein labeling was performed as described previously (Choi et al., 2010) using Alexa
485 Fluor 555 as donor fluorophore and Alexa Fluor 647 as acceptor fluorophore (Invitrogen Life
486 Technologies #A-20346 and #A20347). For symmetric inter-subunit smFRET and for intra-
487 subunit smFRET, donor and acceptor fluorophores were mixed in a 1:1 ratio before adding to the
488 protein. For asymmetric inter-subunit smFRET, two different ctSTIM1 cysteine mutants were
489 mixed separately with donor or acceptor fluorophores, to be recombined afterward into ctSTIM1
490 heterodimers. Labeling efficiency assessed by absorption photometry was typically ~70% but

491 varied for different locations; cysteine mutants with labeling efficiency below 50% were not
492 used for smFRET experiments.
493 For recombination of asymmetric inter-subunit samples, labeled ctSTIM1 homodimers
494 were denatured by adding urea to a concentration of 8 M. Donor and acceptor species were then
495 mixed in a 1:1 ratio, and refolding was allowed to take place during slow dialysis as described
496 above, resulting in a mixture containing 50% ctSTIM1 heterodimers. ctSTIM1 heterodimers
497 with a single donor and a single acceptor fluorophore were individually selected during posthoc
498 analysis of the smFRET experiments.
499
500 **Sample preparation.** Flow cells for single-molecule fluorescence imaging were prepared
501 according to established protocols (Roy et al., 2008). Briefly, strips of double-sided tape were
502 put on a quartz microscope slide (Finkenbeiner) to form channel walls, with holes at the ends of
503 each channel to create entry and exit points for buffer solutions. A microscope coverslip (Erie
504 Scientific #24X40 1.5 001) was pressed on the tape strips and edges of the channels were sealed
505 with two-component epoxy glue. For liposome experiments channels were coated with BSA-
506 biotin (Sigma Aldrich #A8549). For direct surface attachment microscope slides and coverslips
507 were coated with a 100:1 PEG/PEG-biotin mixture (Laysan Bio #BIO-PEG-SVA-5K & MPEG-
508 SVA-5K) prior to flow cell construction. Neutravidin (Thermo Fisher CWA #31000) was
509 flushed into the channels before loading the protein samples. 20/150 TBS (150 mM NaCl, 20
510 mM Tris, pH 7.4 with HCl) was used for rinsing in between steps.
511 For liposome encapsulation of fluorophore-labeled protein samples, biotinylated lipids
512 (18:1 Biotinyl Cap PE, Avanti Polar Lipids #870273C) were mixed with egg-PC lipids (Avanti
513 Polar Lipids #840051C) in a 1:100 ratio. Lipids were suspended in sample buffer and the

514 mixture was passed back-and-forth (Extruder Set, Avanti Polar Lipids #610023) through a
515 liposome extrusion membrane (PC Membranes 0.1µm, Avanti Polar Lipids #610005-1EA).
516 Liposomes were separated from free protein on a Sepharose® CL-4B column (Sigma Aldrich
517 #CL4B200). The conditions resulted in on average <<1 ctSTIM1 dimer per liposome.
518 For direct surface attachment, biotinylated ctSTIM1 samples were diluted to a
519 concentration of ~100 pM and flushed into a PEG-coated, neutravidin-treated channel.
520 Immediately prior to fluorescence imaging, channels were filled with 20/150 TBS containing
521 100 µM cyclooctatetraene (Sigma Aldrich #138924) (COT) and an oxygen scavenging system
522 consisting of 1% D-glucose, 1 mg/ml glucose oxidase (Sigma Aldrich #G2133), and 0.04 mg/ml
523 catalase (Sigma Aldrich #C9322).
524
525 **TIRF microscopy and smFRET measurements.** Single-molecule FRET recordings were
526 performed using a home-built through-the-objective total internal reflection fluorescence (TIRF)
527 imaging system based on a Zeiss Axiovert S100 TV microscope. Alexa Fluor 555 (donor) and
528 Alexa Fluor 647 (acceptor) fluorophores were excited by 532 and 637 nm wavelength lasers
529 (OBIS 532 nm LS 150 mW, Coherent #1280719 and OBIS 637 nm LX 140 mW, Coherent
530 #1196626). A Fluar 100x 1.45 NA oil-immersion objective (Zeiss) was used to establish TIR
531 excitation and collect photon emission. Donor and acceptor emission were separated by a
532 dichroic beamsplitter (Semrock FF652-Di01-25x36) and passed through band-pass filters
533 (Semrock FF01-580/60-25-D for donor emission and Semrock FF01-731/137-25 for acceptor
534 emission) mounted in an OptoSplit-II (Cairn Research), projecting the images side-by-side onto
535 an EM-CCD camera (iXon DU897E, Andor). Hardware and image acquisition were controlled

536 by BeanShell scripts from μManager (Edelstein et al., 2010), and image sequences were stored as
537 stacked TIFF files.
538 Prior to image acquisition, the channel surface was scanned manually using low-intensity
539 donor excitation to identify a suitable location for smFRET imaging, where the density of
540 fluorescent spots appeared homogeneous and without contamination or aggregations. Donor and
541 acceptor emission were then recorded in response to donor excitation, typically for 60 s,
542 immediately followed by 1 s of acceptor excitation to directly identify acceptor fluorophores.
543 Images were acquired in frame-transfer mode with a 100-ms integration time, and laser intensity
544 was set to obtain a trade-off between good signal-to-noise ratio and sufficient active time for
545 both fluorophores (ideally tens of seconds), while inducing fluorophore bleaching within the
546 recording time window. Typically, 10-20 movies were recorded in each of four channels per
547 microscope slide. Measurements were performed at room temperature.
548
549 **smFRET data analysis.** Fluorescence movies were analyzed using custom Python scripts.
550 Donor and acceptor images were aligned using pre-recorded registration images, and fluorescing
551 molecules were identified in the donor and acceptor channels by detecting local signal maxima
552 within a five-pixel-diameter neighborhood. Donor signals that could not be matched to any
553 acceptor signal were discarded. Pixel values for each molecule were summed, and signals from
554 sequential movie frames were stacked to construct the fluorescence time series for each
555 molecule. The local background for each molecule was determined by calculating the median
556 background value within a circular 35-pixel-diameter region in each frame and subtracting it
557 from the raw fluorescence signal. Leakage of donor signal into the acceptor channel in our

558 system was approximately seven percent of the measured donor signal and was systematically
559 subtracted from the measured acceptor signal.

560 γ correction was used to correct for differences in photon emission and detection
561 probabilities of donor and acceptor fluorophores. The value of γ was empirically determined for
562 each individual molecule (McCann et al., 2010), and the correction was applied by multiplying
563 the donor fluorescence signal by γ before calculating the smFRET ratio. The average value from
564 all 12,252 molecules was $\gamma = 1.1$.

565 Traces were selected for final analysis if all of the following criteria were met: (1) the
566 signal-to-noise ratio was equal or greater than five; (2) the acceptor bleached in a single step
567 before the donor bleached; (3) the γ factor was between 0.5 and 2.5; (4) any spontaneous
568 fluctuations of donor and acceptor fluorescence were negatively correlated; and (5) if a donor
569 bleach event was recorded, it occurred in a single step.

570 The FRET ratio E was calculated for each point in the donor and acceptor fluorescence
571 traces (respectively I_D and I_A) where donor and acceptor were both active as $E = I_A/(I_A + \gamma I_D)$. A
572 FRET histogram was constructed for each trace by distributing FRET amplitudes into 50 bins in
573 a [-0.25, 1.25] range. Histograms were normalized by dividing each bin by the total number of
574 FRET points in the trace. An ensemble histogram for multiple molecules was constructed by
575 summing the normalized histograms of the individual traces and dividing each bin by the total
576 number of molecules.

577 The part of the fluorescence traces where both donor and acceptor were active were
578 parameterized by fitting a Hidden Markov model (HMM), using routines from the SMART
579 software package (Greenfeld et al., 2012). To determine the optimal kinetic model, the Bayesian
580 information criterium (BIC) was used to select between models with different numbers of states.

581 To compare FRET levels between different molecules in an ensemble, each HMM state was
582 assigned to a cluster based on its mean FRET value. Clustering was performed based on all
583 observed states in the ensemble, using a k-means algorithm with a predetermined number of
584 target clusters. The number of clusters was determined ad hoc depending on the shape of the
585 FRET histogram. For each cluster the peak of its histogram was reported as its representative
586 FRET level. The predominant FRET cluster was the cluster containing most FRET measurement
587 points.

588 Periods between cluster transitions were used for constructing dwell time histograms.
589 The first and last period of each trace were discarded, so that traces with fewer than two
590 transitions were not included in the dwell time analysis. For transition density plots each
591 transition was described by a coordinate given by the FRET level just before the transition
592 (horizontal axis) and the level after the transition (vertical axis). The local transition density was
593 then calculated on a 50x50 grid ranging from FRET -0.25 to 1.25, by convolution with a
594 Gaussian kernel with two-pixel standard deviation. To prevent individual molecules with many
595 transitions from dominating the plot, each molecule contributed only one data point for each kind
596 of transition. In this way the transition plot reports the number of molecules in which a certain
597 kind of transition appeared.

598

599 **Molecular modeling and simulation.** Molecular dynamics simulations and model optimization
600 procedures were adapted from published procedures (Choi et al., 2010), and performed using
601 Crystallography and NMR System (CNS) (Brunger et al., 1998; Brunger, 2007). Structures were
602 visualized and manipulated using PyMOL (Version 1.8, Schrödinger, LLC.) and ProDy (Bakan
603 et al., 2011). To predict distances between fluorophores, we performed molecular dynamics

604 simulations using atomic models of donor and acceptor fluorophores. Because the structures of
605 Alexa Fluor 555 and Alexa Fluor 647 are not available, we used the structures of the spectrally
606 similar Cy3 and Cy5. Residues of interest on the STIM structure were mutated to cysteine and
607 fluorophore models were covalently attached by CNS. While all protein atoms were held fixed
608 in space, a simulated-annealing protocol sampled possible fluorophore conformations until a
609 local energy minimum was reached. This procedure was repeated 100 times to obtain a
610 distribution of fluorophore orientations, and the average location of the fluorophore center (taken
611 as the location of the CAO atom) was computed from the resulting coordinates. When attached
612 to sites in the CAD crystal structure the overall mean dye center protruded from the Cα atom of
613 the attachment residue by 0.99 ± 0.08 nm for Cy3 and 1.10 ± 0.08 nm for Cy5. Since labeling
614 was stochastic, the donor or acceptor could be on either side in a pair of label sites. To account
615 for this, we averaged Cy3 and Cy5 center coordinates for each residue into a single "effective"
616 center location. Fluorophores were represented in the simulations by a pseudo-atom positioned
617 at this effective center location, and inter-fluorophore distances were then calculated as the
618 distance between two pseudo-atoms.

619 According to Förster theory the distance between donor and acceptor fluorophores (*R*)
620 can be derived from experimentally determined smFRET efficiency (*E*) as $R = R_0 (1/E - 1)^{1/6}$,
621 where R_0 is a proportionality factor reflecting the inter-fluorophore distance at which E = 0.5 (ref
622 (Stryer and Haugland, 1967)). For Alexa Fluor 555 and Alexa Fluor 647 in water, the theoretical
623 value of R_0 is 5.1 nm, assuming fast isotropic re-orientation of the fluorophores. We used this
624 value for calculating smFRET-derived distances.

625 For structural modeling of the CAD apex, we first created a symmetric version of the
626 CAD crystal structure, as the original is slightly asymmetric in the apical region. We copied one

627 subunit and aligned the proximal CC2 (aa 345-378) and CC3 (aa 408-436) domains to the
628 adjacent subunit in the dimer, resulting in a symmetric pair. We then used CNS to allow the
629 apex to relax to a new conformation, guided by smFRET-derived distance constraints (inter-
630 subunit constraints at aa 388, 389, 399, 400, and 401, and intra-subunit constraint 431:389 on
631 both subunits). Helices were treated as rigid bodies, while unstructured regions were treated as
632 flexible chains with variable torsion angles. The distal CC2 helix (aa 379-391) was allowed to
633 rotate around residue G379. During the relaxation of the apex, the proximal CC2 and CC3
634 domains were held fixed in space.

635 To reconstruct the arrangement of CC1 helices around CAD, we used the symmetric
636 CAD structure with smFRET-optimized apical region and modeled CC1 as a chain of
637 dimensionless nodes using custom Python code. Each node on the chain represented the center
638 of a CC1 residue. CC1 chains were generated starting from aa 344 at the CAD N-terminus, by
639 progressively connecting new nodes until the final residue aa 233 was reached. In unstructured
640 regions, nodes were spaced every 0.38 nm and were generated at random angles ≥90°. Alpha-
641 helical regions were modeled as a straight chain of nodes at 0.15 nm intervals. To create a
642 symmetric pair of CC1 chains, nodes were generated for one subunit, and then copied and
643 mirrored in CAD's symmetry planes to create the chain for the other subunit. Each node was
644 subjected to two criteria: (1) it cannot overlap with any residues in CC1 or CAD (volume
645 exclusion in a 0.5 nm-radius sphere), and (2) it must obey smFRET-derived distance (D_{FRET})
646 constraints. Fluorophores positions were not explicitly modeled on the CC1 chains but were
647 accounted for by setting CC1:CC1′ distance constraints to the range of D_{FRET} to D_{FRET} - 2 nm,
648 due to fluorophores extending up to 1 nm on both sides of the helix backbone. Because
649 fluorophores were explicitly modeled in CAD, CC1:CAD distance constraints of D_{FRET} to D_{FRET}

650 - 1 nm were applied. In cases of very high or very low FRET the margins were occasionally
651 relaxed to account for the lack of sensitivity of the smFRET method at these extremes (see
652 Supplementary Figure 4a for a table of all distance constraints used for the CC1:CAD model). If
653 both criteria were met, the node was retained; otherwise it was rejected, and a new node was
654 generated. If no suitable node was found, a new search was started for the preceding node. This
655 process continued until the final N-terminal residue of CC1 (aa 233) was reached, and the
656 resulting model was then stored. Solutions obtained in this way together defined a solution space
657 within which CC1 obeyed the imposed constraints. We used the average of 50 solutions as a
658 model for presentation (Figure 5 and Supplementary Figure 4).
659 To obtain a more detailed picture for the molecular interface of the CC1α1-CAD
660 complex, we aligned the crystal structure of the CC1α1 helical segment (aa 246-271) to the
661 smFRET-derived CC1 model, directing the hydrophobic sidechains to point toward CAD.
662 Residue A419 in the CAD crystal structure was mutated back to the original valine using Pymol.
663 The CC1α1 helix was then docked onto CC3 using the flexpepdock server of Rosetta (London et
664 al., 2011), which performed a molecular dynamics simulation with a fully flexible backbone. An
665 initial docking was performed with distance constraints (2.5 ± 2.5 Å) between CG atoms of
666 residue pairs L248:L416, L251:L416, L258:L423, and L261:L427, which were directly apposed
667 in the smFRET-derived model. This was followed by an unconstrained simulation to obtain the
668 final model (Figure 5e).
669
670 **Chemical crosslinking and mass spectrometry.** For BS^3 crosslinking of ctSTIM1, buffer was
671 changed from Tris- to HEPES-based (150 mM NaCl, 20 mM HEPES (pH 8.0 with NaOH))
672 during the ion exchange procedure. ctSTIM1 samples at 10 μM (~1 mg/ml) were allowed to

673 incubate with 0, 20 and 50 μM BS^3 (BS^3-d0, Sigma Aldrich #21590 or BS^3-d4, Sigma Aldrich
674 #21595) for 30 min at room temperature. The reaction was then quenched for 15 min at room
675 temperature with 20 mM Tris.

676 For crosslinking with EDC, the buffer was changed from Tris- to MES-based (250 mM
677 NaCl, 100 mM MES, pH 6.0 with HCl) during the ion exchange procedure. To increase
678 crosslinking efficiency, EDC (Sigma Aldrich #77149) was used in combination with sulfo-NHS
679 (Sigma Aldrich #24520) to convert carboxyl groups into stable amine-reactive sulfo-NHS esters.
680 ctSTIM1 samples at 100 μM (~10 mg/ml) were allowed to incubate with 0/0, 20/62, 50/156 and
681 100/312 mM EDC/sulfo-NHS for 15 min at room temperature. Two volumes of PBS (250 mM
682 NaCl, 100 mM Na_2HPO_4, pH 8.5 with NaOH) with 25 mM BME (pH 8.5) were then slowly
683 added to quench the EDC and increase the pH for the subsequent amine reaction, incubated 2 h
684 at room temperature and quenched with 40 mM Tris.

685 Crosslinked ctSTIM1 samples were run on SDS-PAGE gels, and monomer and dimer
686 bands were cut and analyzed separately by mass spectrometry. For comparative BS^3
687 crosslinking experiments, BS^3-d0- and BS^3-d4-treated samples were first mixed 1:1 before
688 electrophoresis. Gel bands at 20 and 50 μM BS^3 were combined for analysis (Supplementary
689 Figure 5). For EDC experiments, the monomer band at 10 mM EDC and the combined dimer
690 bands at 2, 5, and 10 mM were used (Supplementary Figure 6).

691 Mass spectrometry analysis of cross-linked samples was performed as described
692 previously (Komolov et al., 2017). Briefly, gel bands were diced into 1x1 mm squares, reduced
693 in 5 mM DTT at 55ºC for 30 min, and then alkylated with 10 mM acrylamide for 30 min at room
694 temperature to cap uncrosslinked cysteines. Following alkylation of free cysteines and washing
695 of gel pieces, proteolytic digestion was completed using trypsin/LysC protease (Promega) in the

696 presence of ProteaseMax (Promega) overnight at 37ºC. Peptides were then extracted and dried
697 under SpeedVac prior to LC/MS analysis.
698 Mass spectrometry experiments were performed using an Orbitrap Fusion Tribrid mass
699 spectrometer (Thermo Scientific, San Jose, CA) with an Acquity M-Class UPLC system (Waters
700 Corporation, Milford, MA) for reverse phase separations. The column was an in-house pulled-
701 and-packed fused silica column with an I.D. of 100 microns pulled to a nanospray emitter.
702 Packing material for the column was C18 reprosil Pur 1.8 micron stationary phase (Dr. Maisch)
703 with a total length of ~25 cm. The UPLC system was set to a flow rate of 300 nL/min, where
704 mobile phase A was 0.2% formic acid in water and mobile phase B was 0.2% formic acid in
705 acetonitrile. Gel-extracted peptides were directly injected onto the column with a gradient of 2-
706 45% mobile phase B, followed by a high-B wash over a total 90 minutes. The mass
707 spectrometer was operated in a data-dependent mode using HCD/ETD decision-tree
708 fragmentation in the orbitrap (HCD) or ion trap (ETD) for MS/MS spectral generation.
709 The collected mass spectra were analyzed using Byonic v 2.12.0 or v2.14.27 (Protein
710 Metrics) as the search engine for peptide ID and protein inference. The precursor and fragment
711 ion tolerance were both set to 12 ppm and 0.4 Da for HCD and ETD, respectively. The search
712 assumed tryptic digestion and allowed for up to two missed cleavages. Potential crosslinked
713 peptides were identified using Byonic's xlink feature, allowing for linker mass where
714 appropriate. Data were validated using the standard reverse-decoy technique at a 1% false
715 discovery rate, and inspected using Byologic for crosslink verification and assessment.
716
717 **Cysteine crosslinking.** Symmetric inter-subunit ctSTIM1 dimers (5 μM) were incubated with
718 300 μM $CuSO_4$ and 900 μM o-phenanthroline for 15 min at room temperature, after which the

719 reaction was quenched with 2x LDS buffer containing 50 mM EDTA. After samples were run
720 on an SDS-PAGE gel and stained with Coomassie Blue, gels were destained and scanned with a
721 LI-COR Odyssey infrared imaging system. Crosslinking efficiency was quantified by the
722 integrated intensity of the dimer band as a fraction of the summed intensities of the monomer and
723 dimer bands.

724 For crosslinking flSTIM1 *in situ*, HEK293 cells were transfected with mCh-STIM1-
725 C437S constructs with selected residues replaced by cysteine. 48 h after transfection, cells were
726 exposed to 0.2 mM diamide for 10 min in either 2 Ca Ringer's (full Ca^{2+} stores) or in 0 Ca^{2+} + 1
727 mM EGTA + 20 μM cyclopiazonic acid (depleted Ca^{2+} stores; CPA, Sigma). Cells were then
728 lysed in RIPA containing 20 mM NEM, protease inhibitor cocktail (Cell Signaling Technology,
729 #5871S) and EDTA. Samples were run on SDS-PAGE and analyzed by Western blot using
730 mouse anti-mCherry primary antibody (1:2000, Takara Bio #632543) and Licor secondary
731 antibody (Licor #926032212) on a LI-COR Odyssey imaging system. 50 mM DTT was added to
732 duplicate samples to test for disulfide crosslinks.

733

734 **Calcium imaging.** For experiments with STIM1 fragments (Supplementary Figure 7), HEK293
735 cells were transfected with mCherry-labeled STIM1 cytosolic fragments (0.25 μg + 0.25 μg
736 empty pcDNA3 vector) and Orai1-GFP (0.5 μg) in a 35-mm dish using lipofectamine2000.
737 Transfected cells were grown overnight in DMEM supplemented with Glutamax, 10% FBS,
738 pen/strep, and 20 μM $LaCl_3$ to minimize the toxic effects of constitutive Ca^{2+} influx. Cells were
739 loaded with 1 μg/ml fura-2/AM for 30 min at room temperature, rinsed, and plated on poly-D-
740 lysine-coated coverslips for imaging.

741 For experiments with flSTIM1, HEK293 cells were transfected with flSTIM1 cysteine
742 mutants with Orai1-GFP. 24-48 h after transfection, cells were loaded with 1 μM fura-2/AM for
743 30 min at room temperature, rinsed, and plated on poly-D-lysine treated coverslip chambers.
744 Fura-2 imaging was conducted using a Zeiss 200M inverted microscope with a Fluar 40X
745 NA 1.3 objective; cells were excited alternately at 350 and 380 nm (Polychrome II, TILL
746 Photonics) and emission at 534 ± 30 nm (FF02-534/30-25, Semrock) or >480 nm (Chroma) was
747 collected with a Flash4.0 sCMOS camera (Hamamatsu Corp.) with 2x2 binning. Images were
748 background corrected before calculation of the 350/380 ratio for each individual cell. Standard
749 bath solution contained (in mM): 155 NaCl, 4.5 KCl, 2 $CaCl_2$, 1 $MgCl_2$, 10 D-glucose and 5 Na-
750 HEPES (pH 7.4). Ca^{2+}-free solution was prepared by replacing $CaCl_2$ with 2 mM $MgCl_2$ and 1
751 mM EGTA. For cysteine crosslinking experiments, cells were treated with 1 μM ionomycin +
752 0.25 mM diamide in Ca^{2+}-free Ringer's followed by Ca^{2+}-free Ringer's + 0.25 mM diamide +
753 0.1% BSA to wash out ionomycin prior to readding standard (2 mM Ca^{2+}) Ringer's + 0.1% BSA.

Acknowledgements

The authors thank members of the Lewis lab for helpful discussions during the course of this project. This work was supported by NIH grant R37GM45374, the Mathers Charitable Foundation, and a Stanford Medicine Discovery Innovation Award (R.S.L.), and by NIH grant R37MH63105 (A.T.B.). S.v.D. was supported by Rubicon postdoctoral fellowship 825.13.027 from the Dutch Research Council NWO, and postdoctoral fellowship 16POST30780015 from the American Heart Association. Mass spectrometry was performed in collaboration with the Vincent Coates Foundation Mass Spectrometry Laboratory, Stanford University Mass Spectrometry. We thank R. Leib and K. Singhal for mass spectrometry analysis of crosslinked STIM1. The work was supported in part by NIH P30 CA124435 utilizing the Stanford Cancer Institute Proteomics/Mass Spectrometry Shared Resource.

Competing interests

The authors declare no competing interests.

768 **References**

769 Bakan, A., L.M. Meireles, and I. Bahar. 2011. ProDy: Protein dynamics inferred from theory and
770 experiments. *Bioinformatics*. 27:1575–1577. doi:10.1093/bioinformatics/btr168.

771 Böhm, J., and J. Laporte. 2018. Gain-of-function mutations in STIM1 and ORAI1 causing
772 tubular aggregate myopathy and Stormorken syndrome. *Cell Calcium*. 76:1–9.
773 doi:10.1016/j.ceca.2018.07.008.

774 Brunger, A.T. 2007. Version 1.2 of the Crystallography and NMR system. *Nature protocols*.
775 2:2728–33. doi:10.1038/nprot.2007.406.

776 Brunger, A.T., P.D. Adams, G.M. Clore, W.L. Delano, P. Gros, R.W. Grossekunstleve, J.S.
777 Jiang, J. Kuszewski, M. Nilges, N.S. Pannu, R.J. Read, L.M. Rice, T. Simonson, and G.L.
778 Warren. 1998. Crystallography & NMR system: A new software suite for macromolecular
779 structure determination. *Acta Crystallographica Section D: Biological Crystallography*.
780 54:905–921. doi:10.1107/S0907444998003254.

781 Brunger, A.T., P. Strop, M. Vrljic, S. Chu, and K.R. Weninger. 2011. Three-dimensional
782 molecular modeling with single molecule FRET. *J Struct Biol*. 173:497–505.
783 doi:10.1016/j.jsb.2010.09.004.

784 Butorac, C., M. Muik, I. Derler, M. Stadlbauer, V. Lunz, A. Krizova, S. Lindinger, R. Schober, I.
785 Frischauf, R. Bhardwaj, M. Hediger, K. Groschner, and C. Romanin. 2019. A novel
786 STIM1-Orai1 gating interface essential for CRAC channel activation. *Cell Calcium*. 79:57–
787 67. doi:S0143416019300156.

788 Calloway, N.T., D.A. Holowka, and B.A. Baird. 2010. A basic sequence in STIM1 promotes
789 Ca2+ influx by interacting with the C-terminal acidic coiled-coil of Orai1. *Biochemistry*.
790 49:1067–1071. doi:10.1021/bi901936q.

791 Choi, U.B., P. Strop, M. Vrljic, S. Chu, A.T. Brunger, and K.R. Weninger. 2010. Single-
792 molecule FRET-derived model of the synaptotagmin 1-SNARE fusion complex. *Nat Struct*
793 *Mol Biol*. 17:318–324. doi:10.1038/nsmb.1763.
794 Covington, E.D., M.M. Wu, and R.S. Lewis. 2010. Essential role for the CRAC activation
795 domain in store-dependent oligomerization of STIM1. *Mol Biol Cell*. 21:1897–1907.
796 doi:10.1091/mbc.E10-02-0145.
797 Cui, B., X. Yang, S. Li, Z. Lin, Z. Wang, C. Dong, and Y. Shen. 2013. The inhibitory helix
798 controls the intramolecular conformational switching of the C-terminus of STIM1. *PLoS*
799 *One*. 8:e74735. doi:10.1371/journal.pone.0074735.
800 Edelstein, A., N. Amodaj, K. Hoover, R. Vale, and N. Stuurman. 2010. Computer control of
801 microscopes using µManager. *Current protocols in molecular biology*. 14:20.1-20.17.
802 doi:10.1002/0471142727.mb1420s92.
803 Fahrner, M., M. Muik, R. Schindl, C. Butorac, P. Stathopulos, L. Zheng, I. Jardin, M. Ikura, and
804 C. Romanin. 2014. A coiled-coil clamp controls both conformation and clustering of
805 stromal interaction molecule 1 (STIM1). *J Biol Chem*. 289:33231–33244.
806 doi:10.1074/jbc.M114.610022.
807 Fahrner, M., M. Stadlbauer, M. Muik, P. Rathner, P. Stathopulos, M. Ikura, N. Müller, and C.
808 Romanin. 2018. A dual mechanism promotes switching of the Stormorken STIM1 R304W
809 mutant into the activated state. *Nat Commun*. 9:825. doi:10.1038/s41467-018-03062-w.
810 Greenfeld, M., D.S. Pavlichin, H. Mabuchi, and D. Herschlag. 2012. Single Molecule Analysis
811 Research Tool (SMART): an integrated approach for analyzing single molecule data. *PLoS*
812 *One*. 7:e30024. doi:10.1371/journal.pone.0030024.
813 Grünberg, R., M. Nilges, and J. Leckner. 2006. Flexibility and Conformational Entropy in

814 Protein-Protein Binding. *Structure*. 14:683–693. doi:10.1016/j.str.2006.01.014.
815 Harrison, S.C. 2008. Viral membrane fusion. *Nature Structural and Molecular Biology*. 15:690–
816 698. doi:10.1038/nsmb.1456.
817 Hirve, N., V. Rajanikanth, P.G. Hogan, and A. Gudlur. 2018. Coiled-coil formation conveys a
818 STIM1 signal from ER lumen to cytoplasm. *Cell Rep*. 22:72–83.
819 doi:10.1016/j.celrep.2017.12.030.
820 Kawasaki, T., I. Lange, and S. Feske. 2009. A minimal regulatory domain in the C terminus of
821 STIM1 binds to and activates ORAI1 CRAC channels. *Biochem Biophys Res Commun*.
822 385:49–54. doi:10.1016/j.bbrc.2009.05.020.
823 Komolov, K.E., Y. Du, N.M. Duc, R.M. Betz, J.P.G.L.M. Rodrigues, R.D. Leib, D. Patra, G.
824 Skiniotis, C.M. Adams, R.O. Dror, K.Y. Chung, B.K. Kobilka, and J.L. Benovic. 2017.
825 Structural and Functional Analysis of a β2-Adrenergic Receptor Complex with GRK5. *Cell*.
826 169:407-421.e16. doi:10.1016/j.cell.2017.03.047.
827 Korzeniowski, M.K., I.M. Manjarrés, P. Varnai, and T. Balla. 2010. Activation of STIM1-Orai1
828 involves an intramolecular switching mechanism. *Sci Signal*. 3:ra82.
829 doi:10.1126/scisignal.2001122.
830 Lacruz, R.S., and S. Feske. 2015. Diseases caused by mutations in ORAI1 and STIM1. *Ann NY*
831 *Acad Sci*. 1356:45–79. doi:10.1111/nyas.12938.
832 Liou, J., M. Fivaz, T. Inoue, and T. Meyer. 2007. Live-cell imaging reveals sequential
833 oligomerization and local plasma membrane targeting of stromal interaction molecule 1
834 after Ca^{2+} store depletion. *Proc Natl Acad Sci USA*. 104:9301–9306.
835 London, N., B. Raveh, E. Cohen, G. Fathi, and O. Schueler-Furman. 2011. Rosetta FlexPepDock
836 web server - high resolution modeling of peptide-protein interactions. *Nucleic Acids*

837 *Research*. 39:249–253. doi:10.1093/nar/gkr431.

838 Ma, G., M. Wei, L. He, C. Liu, B. Wu, S.L. Zhang, J. Jing, X. Liang, A. Senes, P. Tan, S. Li, A.
839 Sun, Y. Bi, L. Zhong, H. Si, Y. Shen, M. Li, M.-S. Lee, W. Zhou, J. Wang, Y. Wang, and
840 Y. Zhou. 2015. Inside-out Ca^{2+} signalling prompted by STIM1 conformational switch. *Nat*
841 *Commun*. 6:7826. doi:10.1038/ncomms8826.

842 McCann, J.J., U.B. Choi, L. Zheng, K. Weninger, and M.E. Bowen. 2010. Optimizing methods
843 to recover absolute FRET efficiency from immobilized single molecules. *Biophys J*.
844 99:961–970. doi:10.1016/j.bpj.2010.04.063.

845 Misceo, D., A. Holmgren, W.E. Louch, P.A. Holme, M. Mizobuchi, R.J. Morales, A.M. De
846 Paula, A. Stray-Pedersen, R. Lyle, B. Dalhus, G. Christensen, H. Stormorken, G.E.
847 Tjønnfjord, and E. Frengen. 2014. A Dominant STIM1 Mutation Causes Stormorken
848 Syndrome. *Human Mutation*. 35:556–564. doi:10.1002/humu.22544.

849 Morin, G., N.O. Bruechle, A.R. Singh, C. Knopp, G. Jedraszak, M. Elbracht, D. Brémond-
850 Gignac, K. Hartmann, H. Sevestre, P. Deutz, D. Hérent, P. Nürnberg, B. Roméo, K.
851 Konrad, M. Mathieu-Dramard, J. Oldenburg, E. Bourges-Petit, Y. Shen, K. Zerres, H.
852 Ouadid-Ahidouch, and J. Rochette. 2014. Gain-of-Function Mutation in STIM1 (P.R304W)
853 Is Associated with Stormorken Syndrome. *Hum Mutat*. 35:1221–1232.
854 doi:10.1002/humu.22621.

855 Muik, M., M. Fahrner, I. Derler, R. Schindl, J. Bergsmann, I. Frischauf, K. Groschner, and C.
856 Romanin. 2009. A cytosolic homomerization and a modulatory domain within STIM1 C
857 terminus determine coupling to ORAI1 channels. *J Biol Chem*. 284:8421–8426.
858 doi:10.1074/jbc.C800229200.

859 Muik, M., M. Fahrner, R. Schindl, P. Stathopulos, I. Frischauf, I. Derler, P. Plenk, B. Lackner,

K. Groschner, M. Ikura, and C. Romanin. 2011. STIM1 couples to ORAI1 via an intramolecular transition into an extended conformation. *EMBO J*. 30:1678–1689. doi:10.1038/emboj.2011.79.

Nesin, V., G. Wiley, M. Kousi, E.-C. Ong, T. Lehmann, D.J. Nicholl, M. Suri, N. Shahrizaila, N. Katsanis, P.M. Gaffney, K.J. Wierenga, and L. Tsiokas. 2014. Activating mutations in STIM1 and ORAI1 cause overlapping syndromes of tubular myopathy and congenital miosis. *Proc Natl Acad Sci USA*. 111:4197–4202. doi:10.1073/pnas.1312520111.

Park, C.Y., P.J. Hoover, F.M. Mullins, P. Bachhawat, E.D. Covington, S. Raunser, T. Walz, K.C. Garcia, R.E. Dolmetsch, and R.S. Lewis. 2009. STIM1 clusters and activates CRAC channels via direct binding of a cytosolic domain to Orai1. *Cell*. 136:876–890. doi:10.1016/j.cell.2009.02.014.

Prakriya, M., and R.S. Lewis. 2015. Store-operated calcium channels. *Physiol Rev*. 95:1383–1436. doi:10.1152/physrev.00020.2014.

Qin, M., W. Wang, and D. Thirumalai. 2015. Protein folding guides disulfide bond formation. *Proc Natl Acad Sci USA*. 112:11241–11246. doi:10.1073/pnas.1503909112.

Rappsilber, J. 2011. The beginning of a beautiful friendship: cross-linking/mass spectrometry and modelling of proteins and multi-protein complexes. *J Struct Biol*. 173:530–540. doi:10.1016/j.jsb.2010.10.014.

Rathner, P., M. Fahrner, L. Cerofolini, H. Grabmayr, F. Horvath, H. Krobath, A. Gupta, E. Ravera, M. Fragai, M. Bechmann, T. Renger, C. Luchinat, C. Romanin, and N. Müller. 2020. Interhelical interactions within the STIM1 CC1 domain modulate CRAC channel activation. *Nature Chemical Biology*. doi:10.1038/s41589-020-00672-8.

Roy, R., S. Hohng, and T. Ha. 2008. A practical guide to single-molecule FRET. *Nat Methods*.

883 5:507–516. doi:10.1038/nmeth.1208.
884 Schmidt, C., and C. V Robinson. 2014. A comparative cross-linking strategy to probe
885 conformational changes in protein complexes. *Nat Protoc*. 9:2224–2236.
886 doi:10.1038/nprot.2014.144.
887 Schober, R., D. Bonhenry, V. Lunz, J. Zhu, A. Krizova, I. Frischauf, M. Fahrner, M.Q. Zhang, L.
888 Waldherr, T. Schmidt, I. Derler, P.B. Stathopulos, C. Romanin, R.H. Ettrich, and R.
889 Schindl. 2019. Sequential activation of STIM1 links Ca^{2+} with luminal domain unfolding.
890 *Sci Signal*. 12. doi:10.1126/scisignal.aax3194.
891 Soboloff, J., B.S. Rothberg, M. Madesh, and D.L. Gill. 2012. STIM proteins: dynamic calcium
892 signal transducers. *Nat Rev Mol Cell Biol*. 13:549–565. doi:10.1038/nrm3414.
893 Stathopulos, P., G. Li, M. Plevin, J. Ames, and M. Ikura. 2006. Stored Ca^{2+} depletion-induced
894 oligomerization of STIM1 via the EF-SAM region: An initiation mechanism for capacitive
895 Ca^{2+} entry. *J Biol Chem*. 281:35855–35862.
896 Stathopulos, P.B., R. Schindl, M. Fahrner, L. Zheng, G.M. Gasmi-Seabrook, M. Muik, C.
897 Romanin, and M. Ikura. 2013. STIM1/Orai1 coiled-coil interplay in the regulation of store-
898 operated calcium entry. *Nat Commun*. 4:2963. doi:10.1038/ncomms3963.
899 Stryer, L., and R.P. Haugland. 1967. Energy transfer: a apectroscopic ruler. 58:719–726.
900 Thompson, J.L., Y. Zhao, P.B. Stathopulos, A. Grossfield, and T.J. Shuttleworth. 2018.
901 Phosphorylation-mediated structural changes within the SOAR domain of STIM1 enable
902 specific activation of distinct Orai channels. *J Biol Chem*. 293:3145–3155.
903 doi:10.1074/jbc.M117.819078.
904 Wang, X., Y. Wang, Y. Zhou, E. Hendron, S. Mancarella, M.D. Andrake, B.S. Rothberg, J.
905 Soboloff, and D.L. Gill. 2014. Distinct Orai-coupling domains in STIM1 and STIM2 define

906 the Orai-activating site. *Nat Commun*. 5:3183. doi:10.1038/ncomms4183.

907 Weiss, S. 1999. Fluorescence spectroscopy of single biomolecules. *Science*. 283:1676–1683.
908 doi:10.1126/science.283.5408.1676.

909 Weiss, S. 2000. Measuring conformational dynamics of biomolecules by single molecule
910 fluorescence spectroscopy. *Nature Structural Biology*. 7:724–729. doi:10.1038/78941.

911 Wu, M.M., J. Buchanan, R.M. Luik, and R.S. Lewis. 2006. Ca^{2+} store depletion causes STIM1 to
912 accumulate in ER regions closely associated with the plasma membrane. *J Cell Biol*.
913 174:803–813. doi:10.1083/jcb.200604014.

914 Wu, M.M., E.D. Covington, and R.S. Lewis. 2014. Single-molecule analysis of diffusion and
915 trapping of STIM1 and Orai1 at endoplasmic reticulum-plasma membrane junctions. *Mol*
916 *Biol Cell*. 25:3672–3685. doi:10.1091/mbc.E14-06-1107.

917 Yang, X., H. Jin, X. Cai, S. Li, and Y. Shen. 2012. Structural and mechanistic insights into the
918 activation of Stromal interaction molecule 1 (STIM1). *Proc Natl Acad Sci USA*. 109:5657–
919 5662. doi:10.1073/pnas.1118947109.

920 Yu, F., L. Sun, S. Hubrack, S. Selvaraj, and K. Machaca. 2013. Intramolecular shielding
921 maintains the ER Ca^{2+} sensor STIM1 in an inactive conformation. *J Cell Sci*. 126:2401–
922 2410. doi:10.1242/jcs.117200.

923 Yuan, J., W. Zeng, M. Dorwart, Y. Choi, P. Worley, and S. Muallem. 2009. SOAR and the
924 polybasic STIM1 domains gate and regulate Orai channels. *Nat Cell Biol*. 11:337–343.
925 doi:10.1038/ncb1842.

926 Zhou, Y., P. Srinivasan, S. Razavi, S. Seymour, P. Meraner, A. Gudlur, P.B. Stathopulos, M.
927 Ikura, A. Rao, and P.G. Hogan. 2013. Initial activation of STIM1, the regulator of store-
928 operated calcium entry. *Nat Struct Mol Biol*. 20:973–981. doi:10.1038/nsmb.2625.

929

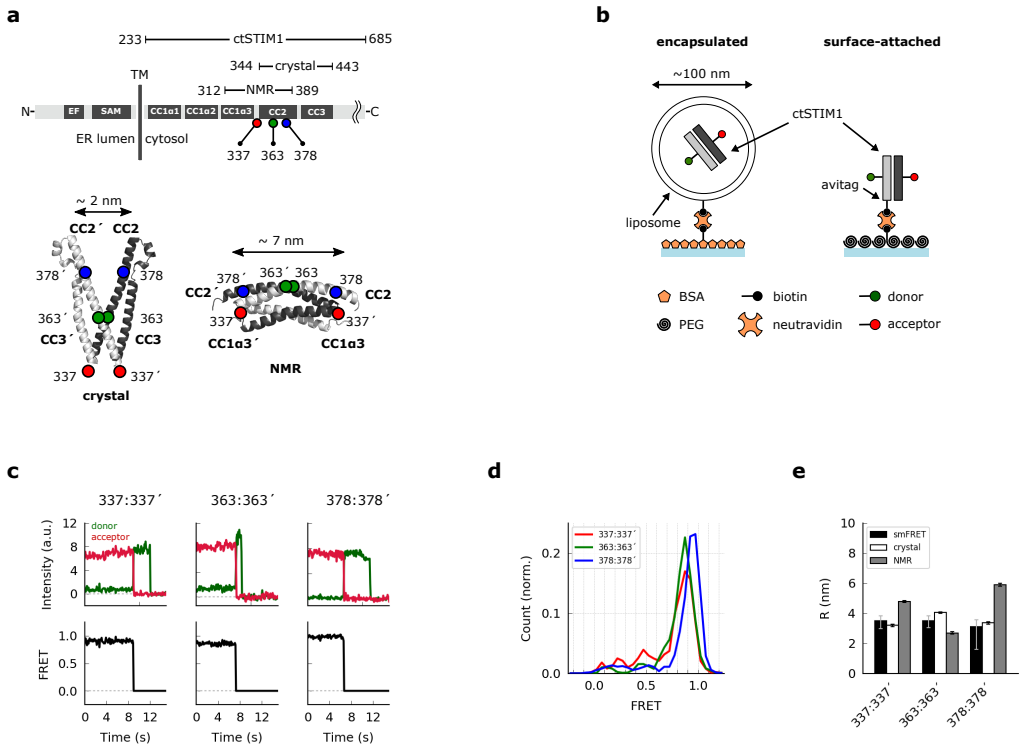

930

931 **Figure 1. Parallel orientation of CC2 domains in ctSTIM1 is consistent with the CAD**

932 **crystal structure.** (**a**) (*top*) Schematic overview of domains in ctSTIM1, comprising the

933 membrane-proximal coiled-coil 1 (CC1) domain (with helical regions α1, α2, and α3), and the

934 CC2 and CC3 domains which are part of CAD. (*bottom*) The orientations of the CC2 domains

935 are a prominent feature that distinguishes the crystal structure of CAD (*bottom left*, parallel CC2

936 domains; 3TEQ.pdb) and the NMR structure of CC1α3-CC2 (*bottom right*, anti-parallel CC2

937 domains; 2MAJ.pdb). Sites tested by inter-subunit smFRET are indicated. Although aa 337 is

938 not part of the crystal structure (aa 344-443), it is sufficiently close to permit comparison to the

939 NMR structure. (**b**) Two methods for immobilizing single ctSTIM1 dimers for smFRET.

940 ctSTIM1 peptides were encapsulated in liposomes and immobilized on a glass slide by a biotin-

941 neutravidin interaction or were attached directly via a C-terminal avitag. (**c**) Example recordings

942 of donor (*green*) and acceptor (*red*) fluorescence evoked by donor excitation for sites 337:337´,

943 363:363′, and 378:378′. Single-step bleaching events indicate a single molecule, while the anti-
944 correlated response of the donor to the acceptor bleach event is a hallmark of smFRET.
945 Calculated instantaneous FRET ratios (*black*) are shown below. (**d**) Ensemble smFRET
946 histograms for sites 337:337′, 363:363′, and 378:378′ displayed predominantly high FRET,
947 indicating close parallel apposition. (**e**) A comparison of smFRET-derived distances (*black*)
948 with simulated inter-fluorophore distances from the crystal (*white*) and NMR structures (*gray*).
949 The measured distances closely match the crystal structure but deviate strongly from the NMR
950 structure, particularly for 337:337′ and 378:378′. smFRET error bars indicate the expected
951 distance deviation corresponding to an uncertainty of ±0.05 in FRET measurement. Simulation
952 error bars indicate the s.e.m. of inter-fluorophore distance from 100 simulations of dye position
953 (see Methods).

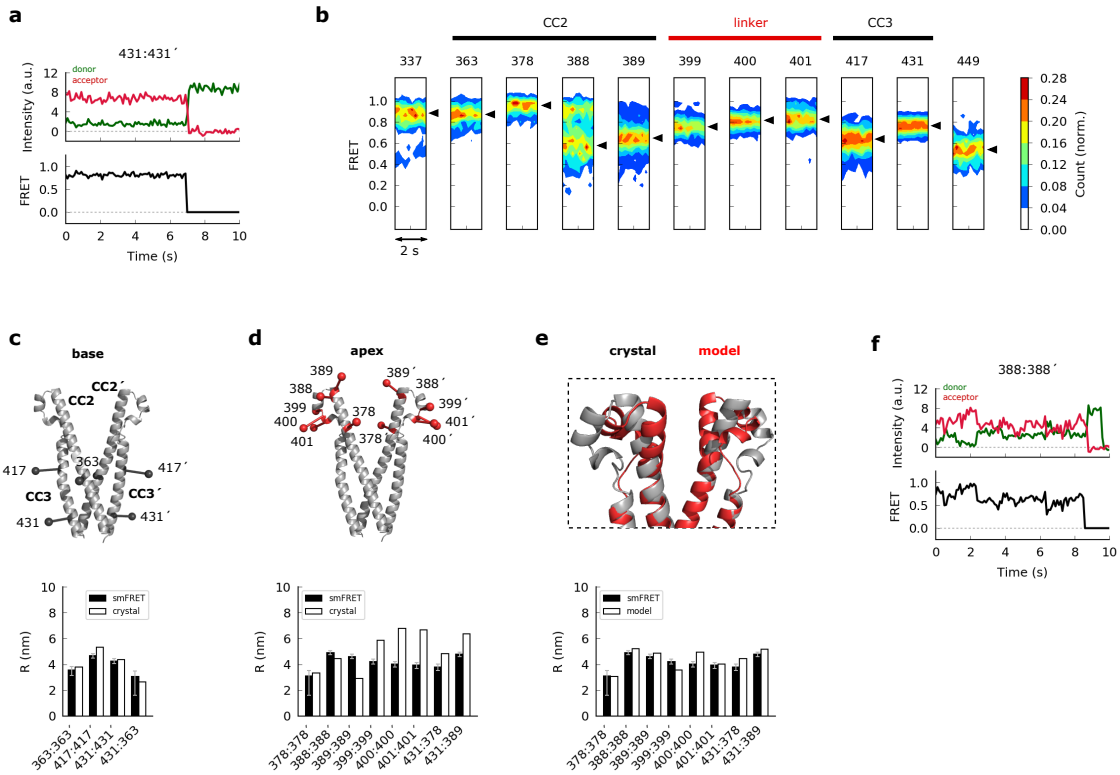

954

955 **Figure 2. The apex of CAD in ctSTIM1 deviates from the CAD crystal structure.** (**a**)
956 Representative smFRET recording at the base of CAD (431:431´) showing stable, high FRET.
957 (**b**) Ensemble density plots of the initial 2 s of inter-subunit smFRET recordings for sites
958 throughout CAD. Predominant FRET levels are shown by arrowheads to the right of each plot.
959 (**c-d**) Comparison of inter-fluorophore distances from smFRET and the CAD crystal structure.
960 Simulated fluorophores were represented by the average position of a central atom, indicated
961 here as ball-on-stick models (see Methods). For sites near the dimer interface (the 'base' of
962 CAD, **c**), the smFRET-derived distances (*black bars)* agree closely with the crystal structure
963 (*white bars*). Measurements in the apex (**d**) deviated from the crystal structure. (**e**) Modified
964 structure (*red*) generated by a smFRET-constrained optimization of the crystal structure (*gray*).
965 Outward rotation of the distal CC2 region (aa 379-391) around G379 as a pivot point restored

966 close correspondence between smFRET-derived distances and the crystal structure (*bottom*). (**f**)

967 Representative example of smFRET fluctuations in the CAD apex (388:388′).

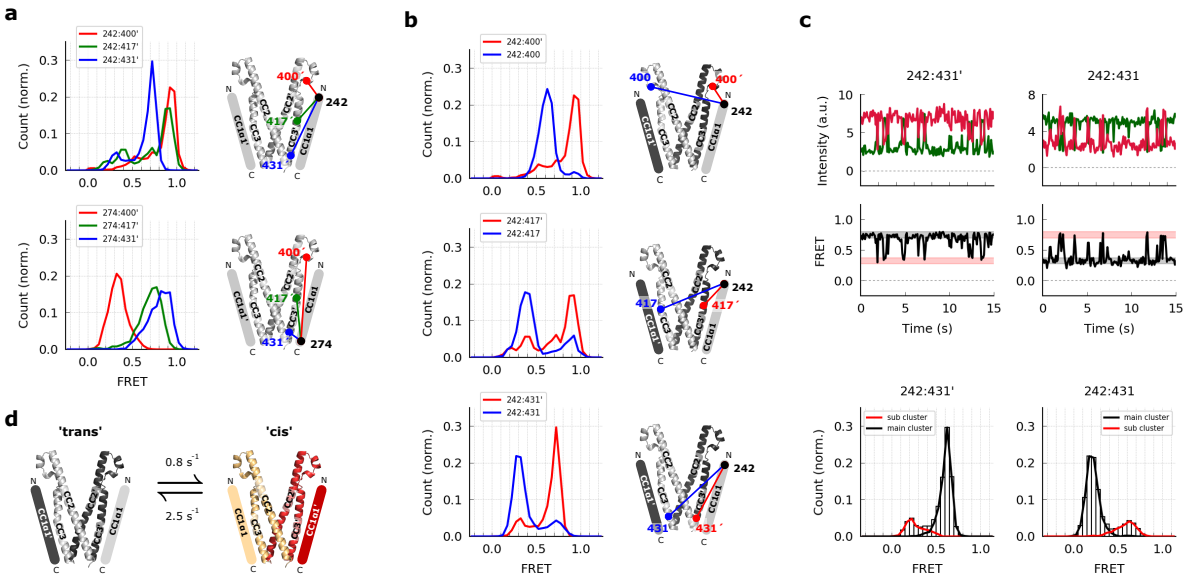

968

969 **Figure 3. The CC1α1 domain is near and parallel to the CC3 domain of the opposing CAD**
970 **subunit.** (**a**) Asymmetric inter-subunit smFRET measurements between CC1α1 and CC3 reveal
971 a parallel orientation, with high FRET levels at 242:400′ (*top, red*) and 274:431′ (*bottom, blue*)
972 indicating close apposition. The crystal structure of CAD is shown with schematic
973 representation of CC1α1 domains. (**b**) The predominant smFRET level between CC1α1 and
974 CC3 was consistently higher for inter-subunit measurements (*red*) than intra-subunit
975 measurements (*blue*). This pattern indicates a predominant domain-swapped configuration in
976 which CC1α1 docks close to the CC3 domain of its opposing subunit. (**c**) Inter- and intra-
977 subunit recordings (242:431′ and 242:431, respectively) displayed brief spontaneous smFRET
978 transitions between two states indicated by red and black bars. In both cases fluctuations
979 occurred between the same two FRET levels, suggesting the CC1α1 domains switched sides on
980 CAD (see also Supplementary Figure 3a). (**d**) Schematic illustration of spontaneous
981 conformational transitions of the CC1α1 domain. In the predominant conformation, CC1α1 is
982 closely apposed and parallel to CC3 on its opposing subunit in a domain-swapped configuration
983 ('trans'). Occasionally, CC1α1 switches to interact briefly with CC3 on its own subunit ('cis').

984 Rate constants were derived from dwell time analysis of smFRET traces (Supplementary Figure

985 3a).

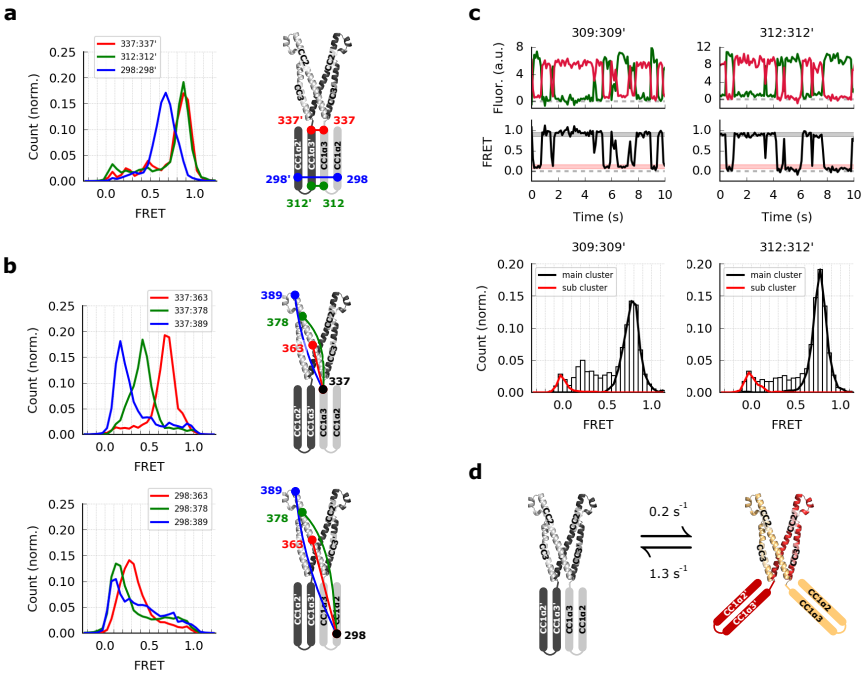

986

987 **Figure 4. The CC1α2 and CC1α3 domains are closely apposed and directed away from**

988 **CAD.** (**a**) High inter-subunit smFRET at the N- and C-termini of the CC1α3 domain (aa 312 and

989 337, respectively) indicates close parallel apposition of the two helices. The crystal structure of

990 CAD is shown with a schematic depiction of CC1α2 and CC1α3 domains. (**b**) (*top*) High intra-

991 subunit smFRET from aa 337 to sites on CC2 declined progressively with distance, while intra-

992 subunit smFRET from aa 298 (near the CC1α2/3 linker) to sites in CC2 was low (*bottom*),

993 indicating that the CC1α2 and α3 domains are directed away from CAD. (**c**) Inter-subunit

994 recordings near the CC1α3 N-terminus showed brief transitions from the predominant high-

995 FRET state to a transient low-FRET state. Ensemble histograms show similar main and transient

996 FRET states for neighboring sites aa 309 and 312. (**d**) Schematic depiction of spontaneous

997 conformational transitions of the CC1α3 domains. CC1α3 domains are predominantly in close

998 parallel apposition (*left*) and occasionally transition to a transient open configuration (*right*).

999 Rate constants were derived from dwell time analysis of smFRET traces (Supplementary Figure

1000 3b).

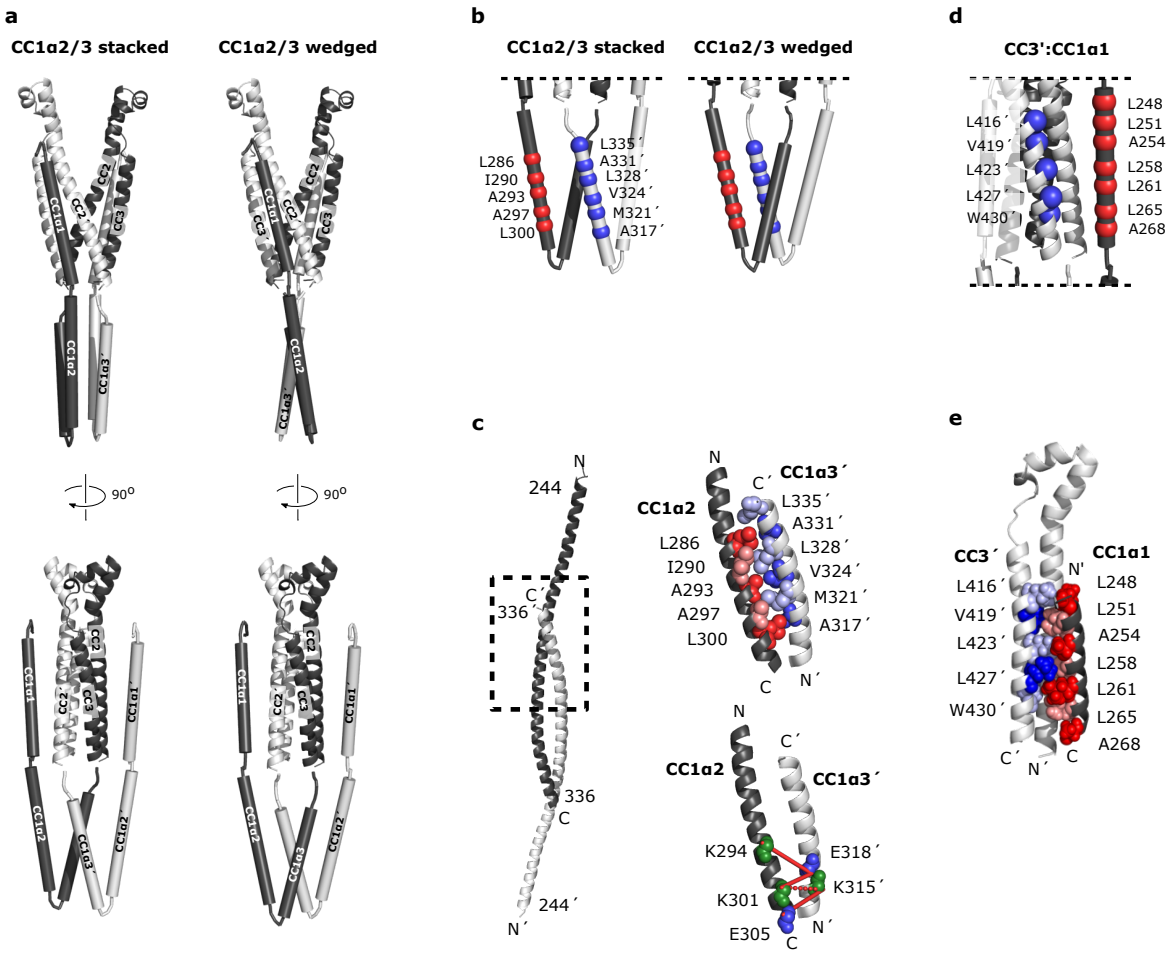

1001

1002 **Figure 5. A model of the configuration of CC1 and CAD in ctSTIM1.** (**a**) 36 smFRET-
1003 derived distances were used to reconstruct the orientations of CC1 domains relative to CAD,
1004 yielding two classes of solutions with the CC1α2/3 domains in a 'stacked' (*left*) or 'wedged'
1005 (*right*) configuration. In both classes, CC1α1 domains are in close parallel apposition to the CC3
1006 domains on the adjacent subunit in a domain-swapped configuration, with the CC1α2 and CC1α3
1007 domains forming a compact parallel structure directed away from CAD. The average of 50
1008 model solutions is shown for each class (see Supplementary Figure 4b for individual solutions).
1009 (**b**) smFRET-derived models suggest hydrophobic stabilization of the CC1α2/3 complex by
1010 antiparallel apposition of CC1α2 and CC1α3´. (**c**) The crystal structure of CC1 peptides defines
1011 an antiparallel interaction of CC1α2/α3´ domains (*left*, *dashed box*), in which heptad-like

1012 hydrophobic sequences form a tightly packed dimer interface (*top right*, adapted from
1013 4O9B.pdb). (*bottom right*) Tight antiparallel packing of CC1α2/α3′ in ctSTIM1 was confirmed
1014 by inter-subunit crosslinks with EDC (*solid lines*) and BS^3 (*dashed line*) (see also Supplementary
1015 Figure 6). (**d**) Parallel apposition of hydrophobic residues on CC1α1 and CC3′. Several of these
1016 were previously identified by mutagenesis to stabilize the inactive state of STIM1, including
1017 L248, L251, L416, and L423. (**e**) A model of the CC1α1:CC3′ interface obtained by
1018 computational peptide docking (see Methods). In the lowest-energy solution, the helices engage
1019 in direct mutual hydrophobic interactions.

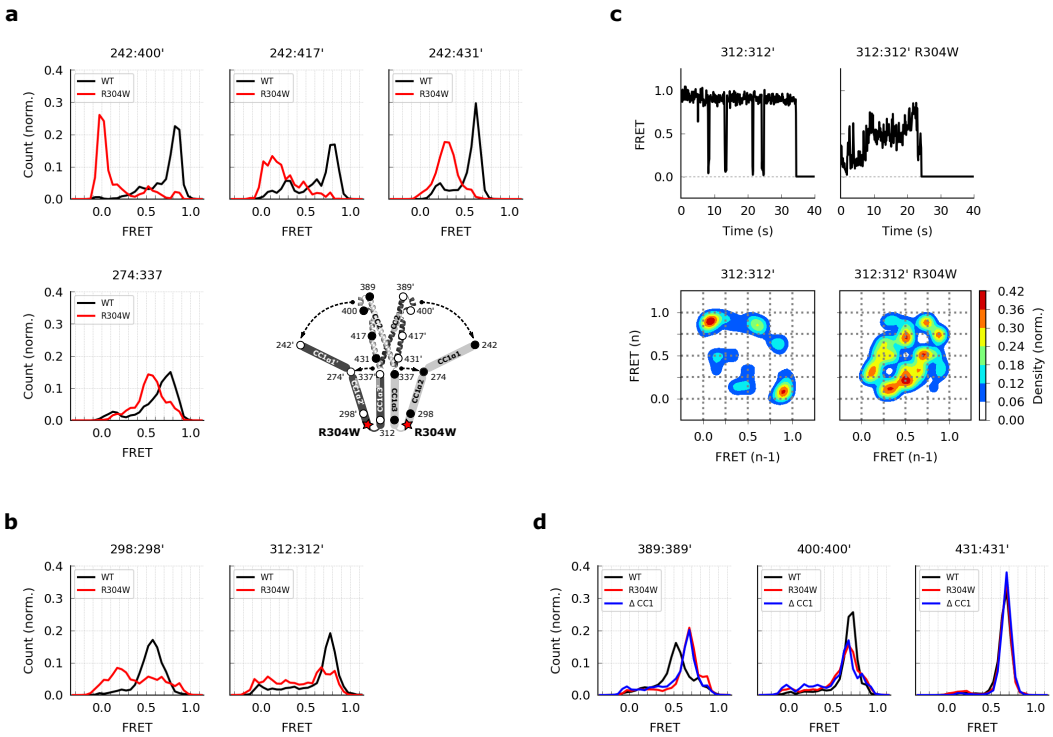

Figure 6. The Stormorken R304W mutation releases CC1 from CAD. (**a**) The R304W mutation reduced inter-subunit smFRET between aa 242 on CC1α1 and sites 400′, 417′, and 431′ on CC3′, indicating separation of CC1α1 from CAD (*top*). The mutation also reduced intra-subunit FRET for 274:337, suggesting a widening of the angle between CC1α2 and CC1α3 (*bottom*). (**b**) The predominant FRET levels for 298:298′ (*left*) and 312:312′ (*right*) were diminished by R304W, suggesting the compact parallel structure of CC1α2/3 domains was disrupted in favor of a dilated, low-FRET state. (**c**) Effects of R304W on inter-subunit FRET fluctuations at 312:312′, near the CC1α3 N-terminus. The dominant large-amplitude fluctuations of the wild-type (*top left*) were entirely absent in the mutant, which instead displayed frequent small fluctuations at a range of FRET levels (*top right*). The different fluctuation modes are summarized in ensemble transition density plots (see Methods) which show a single dominant FRET transition for wild-type molecules (*bottom left*, 38 molecules), and a multimodal density distribution for R304W mutants (*bottom right*, 25 molecules). (**d**) In the

1034 CAD apex, R304W or deletion of the entire CC1 region (ctSTIM1-ΔCC1) increased the FRET at
1035 389:389′ (*left*) and reduced it at 400:400′ (*center*), suggesting that the apex interacts with CC1α1
1036 in the WT conformation. Neither R304W nor ΔCC1 affected FRET at 431:431′ (*right*) in the
1037 CAD base.

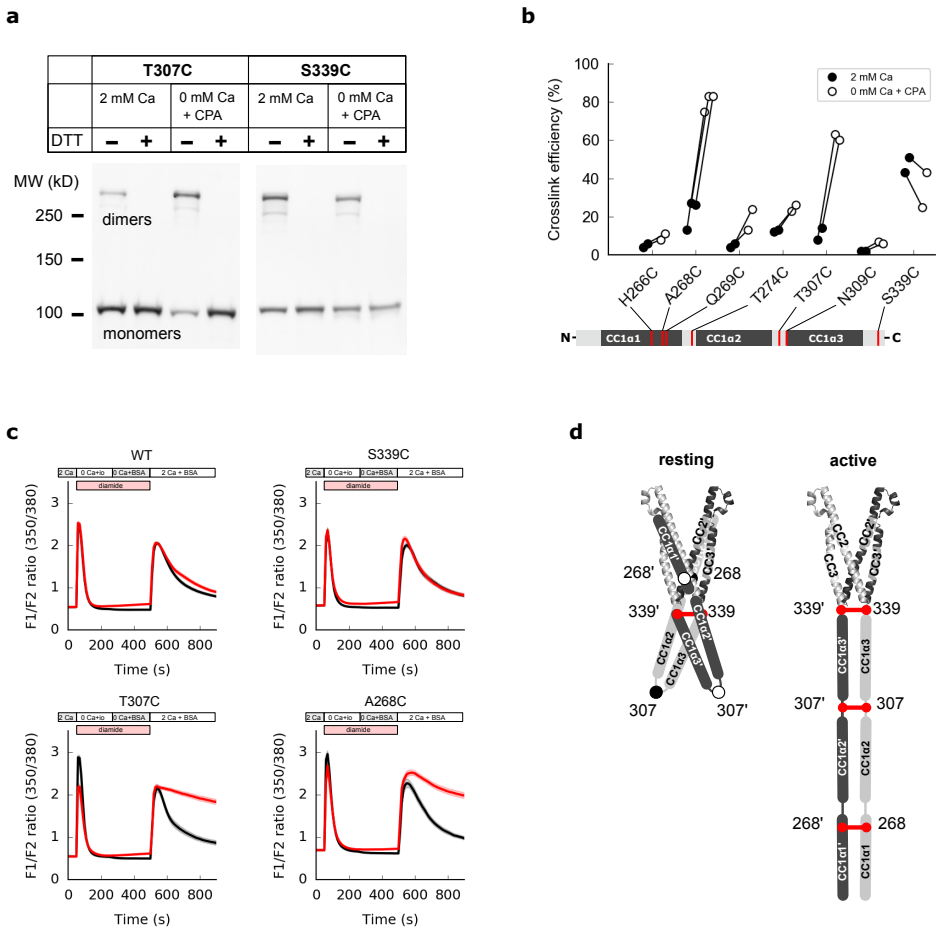

1038

1039 **Figure 7. Close contacts form between CC1 domains along their entire length in the**

1040 **activated state of STIM1.** **(a)** Full-length STIM1 (flSTIM1) mutants were transiently over-

1041 expressed in HEK293 cells for diamide-induced cysteine crosslinking *in vivo*. Western-blot

1042 analysis of cysteine crosslinking of flSTIM1-T307C (*left*) and flSTIM1-S339C (*right*), under

1043 resting (2 mM Ca^{2+}) or store-depleted (0 mM Ca^{2+} + CPA) conditions. (**b**) Summary of flSTIM1

1044 cysteine crosslinking before (*black*) and after (*white*) store depletion measured in individual

1045 paired experiments. While crosslinking at aa 268 and aa 307 strongly increased in the activated

1046 state, crosslinking at aa 339 occurred independent of STIM1 activation (see also **a** and

1047 Supplementary Figure 8b). (**c**) WT flSTIM1 and cysteine mutants were co-expressed with Orai1

1048 for cytosolic calcium imaging (see Methods). For WT flSTIM1 cells, after store depletion by

1049 transient exposure to ionomycin (io), readdition of Ca^{2+} elevated $[Ca^{2+}]_i$ due to SOCE, followed
1050 by a decline as SOCE deactivated from store refilling (*top left, black*). Diamide (*red*) did not
1051 affect the WT response. In contrast, diamide-induced crosslinking of T307C stabilized the active
1052 state, as evidenced by persistent calcium influx after ionomycin wash-out and store refilling
1053 (*bottom left, red*). Similar results were obtained for crosslinking A268C (*bottom right*, see also
1054 Supplementary Figure 8). Crosslinking of S339C did not inhibit deactivation of SOCE upon
1055 store refilling (*top right*). Number of cells (control/diamide): WT (91/106), S339C (44/41),
1056 T307C (38/46), A268C (31/47). (**d**) Schematic illustration of CC1 cysteine crosslinking in the
1057 resting (*left*) and activated (*right*) states of flSTIM1. In the resting conformation, CC1α1 and
1058 CC1α3 domains are kept apart, preventing crosslinking at locations upstream of aa 339. Upon
1059 store depletion, release of the CC1α1 domains from CAD promotes alignment of CC1 domains
1060 along their entire length, enabling crosslinking at aa 268 and 307.

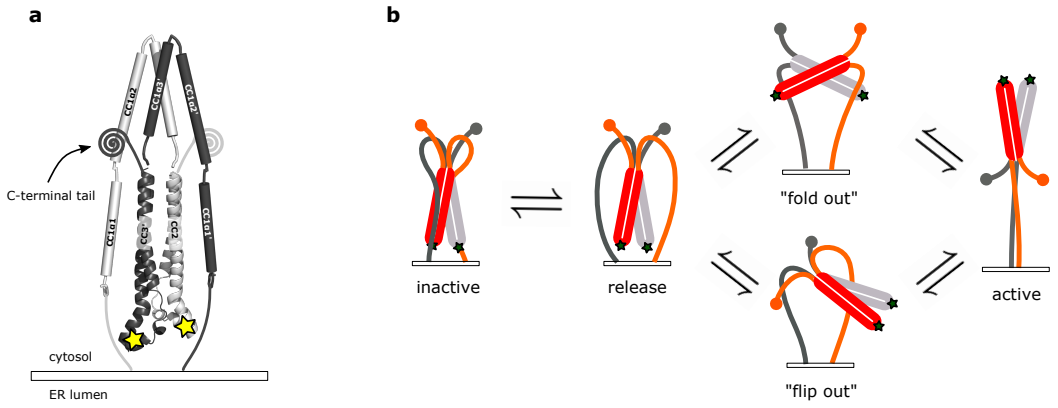

1061

1062 **Figure 8. Possible conformational trajectories of flSTIM1 activation *in vivo*.** (**a**) In the
1063 resting state, the parallel orientation of CC1α1 and CC3 domains implies that CAD is held with
1064 its apex close to and pointed towards the ER membrane, effectively shielding critical interaction
1065 sites (*stars*) from engaging with Orai. The region C-terminal to CAD is abbreviated as its
1066 conformation is not known. (**b**) Alternative models for transitions to the active state of flSTIM1.
1067 In the "fold out" model (*top*), following the release of CC1α1, CAD undergoes a symmetric
1068 conformational change in which the CC2 domains pass through a transient antiparallel state,
1069 providing a free path for the region downstream of CAD to extend towards the plasma
1070 membrane. In the "flip out" model (*bottom*), CAD maintains its parallel resting conformation
1071 and undergoes an asymmetric outward rotation from between the CC1 domains. Assuming that
1072 the initial resting conformation is symmetric, one of its C-terminal domains (*gray*) would have to
1073 be carried through the gap between the two CC1 domains.